MCAT Institute
Progress Report
95-17

Turbomachinery Design and Tonal Acoustics Computations

Akil A. Rangwalla

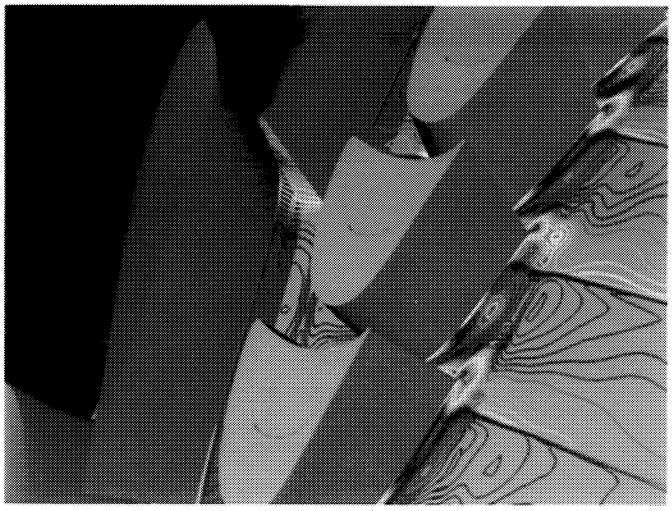

January 1995

NCC2-767

MCAT Institute
3933 Blue Gum Drive
San Jose, CA 95127

Turbomachinery design and tonal acoustics computations

Akil A. Rangwalla

Objective

This report describes work performed under co-operative agreement NCC2-767 with NASA Ames Research Center, during the period from June 1993 to January 1995. The objective of this research was two-fold. The first objective was to complete the three-dimensional unsteady calculations of the flow through a new transonic turbine and study the effects of secondary flows due to the hub and casing, tip clearance vortices and the inherent three-dimensional mixing of the flow. It should be noted that this turbine was and is still in the design phase and the results of the calculations have formed an integral part of the design process. The second objective of this proposal was to evaluate the capability of rotor-stator interaction codes to calculate tonal acoustics.

Motivation

The ultimate motivation behind this proposed research is to be able to simulate a complete propulsion system. In order to do this, certain key CFD methodologies such as turbomachinery flow solvers have to evolve to a level of maturity so as to be used with confidence. An important criterion for a numerical code to be a design tool for turbomachinery applications, is its ability to predict accurately, the secondary flow features, losses and other more sensitive flow quantities such as tonal acoustics.

Background

Computational fluid dynamics (CFD) is playing an increasingly important role in the design of various propulsion components. Considerable progress has already been made in using CFD in the design of turbopumps and impellers. Turbomachinery (rotor-stator) flow solvers have been developed at NASA/ARC which incorporate some of the most modern, high-order upwind-biased schemes for the solution of the thin-layer Navier-Stokes equations (Ref. 1-2). The family of rotor-stator interaction codes (which includes ROTOR-1, ROTOR-2-4 and STAGE-2 codes) are currently in use in several industrial and government organizations. So far, the unsteady rotor codes have proven quite capable of predicting pressure variations on the surface of the airfoils. They have also demonstrated their capability of predicting more "sensitive" flow variables such as the total pressure losses in the flow field. In addition, two-dimensional versions have been used in the actual design of turbomachinery (Ref. 3). However, the success of CFD in the design of turbomachinery has largely been in predicting the two-dimensional time-averaged and unsteady pressure loads on airfoil surfaces. However, there are important three-

dimensional effects in the flow associated with turbomachines such as secondary flows due to the hub and casing, tip clearance vortices and the inherent three-dimensional mixing of the flow which require additional detailed analysis. Additionally, the flow in the tip clearance region is not well understood. There can be considerable flow turning and temperature variation in this region that can affect the overall performance of the turbomachine. An important aspect of the flow in a turbomachine is the impact on the overall losses due to secondary flow features. Hence the timely completion of the three-dimensional unsteady flow in a new transonic turbine in the design stage would make rotor-stator interaction codes developed at NASA/ARC a viable tool for turbomachinery design.

The second aspect of this proposal was the calculation of tonal acoustics in turbomachines. In Ref. 4-5, two-dimensional unsteady rotor-stator interaction calculations were performed to study the plurality of spinning modes that are present in such an interaction. The propagation of these modes in the upstream and downstream regions was analyzed and compared with numerical results. It was found that the numerically calculated tonal acoustics could be affected by the type of numerical boundary conditions employed at the inlet and exit of the computational boundaries and the grid spacing in the upstream and downstream regions. Results in the form of surface pressure amplitudes and the spectra of turbine tones and their far field behavior were presented. The "mode-content" for different harmonics of blade-passage frequency was shown to conform with that predicted by a kinematical analysis. It was however assessed that a similar three-dimensional calculation would require a highly accurate algorithm since relying on very fine grids would be impractical. Also, three-dimensional non-reflective boundary conditions would have to be developed. It was with the above in mind, that the development of a new high-order accurate multi-zone Navier-Stokes code was initiated. This code is based largely on the ideas presented in Ref. 6. Figure 1 shows a comparision of the results obtained by the new code with that obtained from ROTOR-2. These preliminary results look quite promising and have indicated a further study in the development of the new method.

Achievements

Flow predictions in an advanced transonic turbine was completed in a timely fashion. The task for the calculation was given at the same time as fabrication was initiated. The numerical results were obtained well in advance of the first experimental runs and have already played an itegral part in determining the placement of the probes and have also facilitated in the understanding of the experimental results. This exercise has made three-dimensional rotor-stator interaction codes a viable tool in the design process.

A detailed study of the capability of the two-dimensional rotor-stator codes in computing tonal acoustics was completed. In anticipation of extending this capability for three-dimensional predictions, development of a new high-order-accurate flow solver was

initiated. Preliminary results appear to be promising.

References

1. Rai, M. M., "Navier - Stokes Simulations of Rotor-Stator Interaction Using Patched and Overlaid Grids," AIAA Journal of Propulsion and Power, Vol. 3, No. 5, pp. 387-396, Sep. 1987.

2. Rai, M. M., "Three-Dimensional Navier-Stokes Simulations of Turbine Rotor-Stator Interaction; Part 1 & 2," AIAA Journal of Propulsion and Power, Vol. 5, No. 3, pp. 305-319, May-June 1989.

3. Rangwalla, A. A., Madavan, N. K. and Johnson, P. D., "Application of an Unsteady Navier-Stokes Solver to Transonic Turbine Design", AIAA Journal of Propulsion and Power, **8**, 1079-1086, 1992.

4. Rangwalla, A. A. and Rai, M., M. "A kinematical/numerical analysis of rotor-stator interaction noise", AIAA Paper No. 90-0281.

5. Rangwalla, A. A. and Rai, M., M. "A numerical analysis of tonal acoustics in rotor-stator interactions", Journal of Fluids and Structures, **7**, 611-637, 1993.

6. Rai, M. M. and Chakravarthy, S. "Conservative high-order-accurate finite-difference methods for curvilinear grids", AIAA Paper No. 93-3380.

ROTOR/STATOR INTERACTION COMPUTATIONS USING A NEW FOURTH-ORDER ACCURATE METHOD FOR CURVILINEAR GRIDS

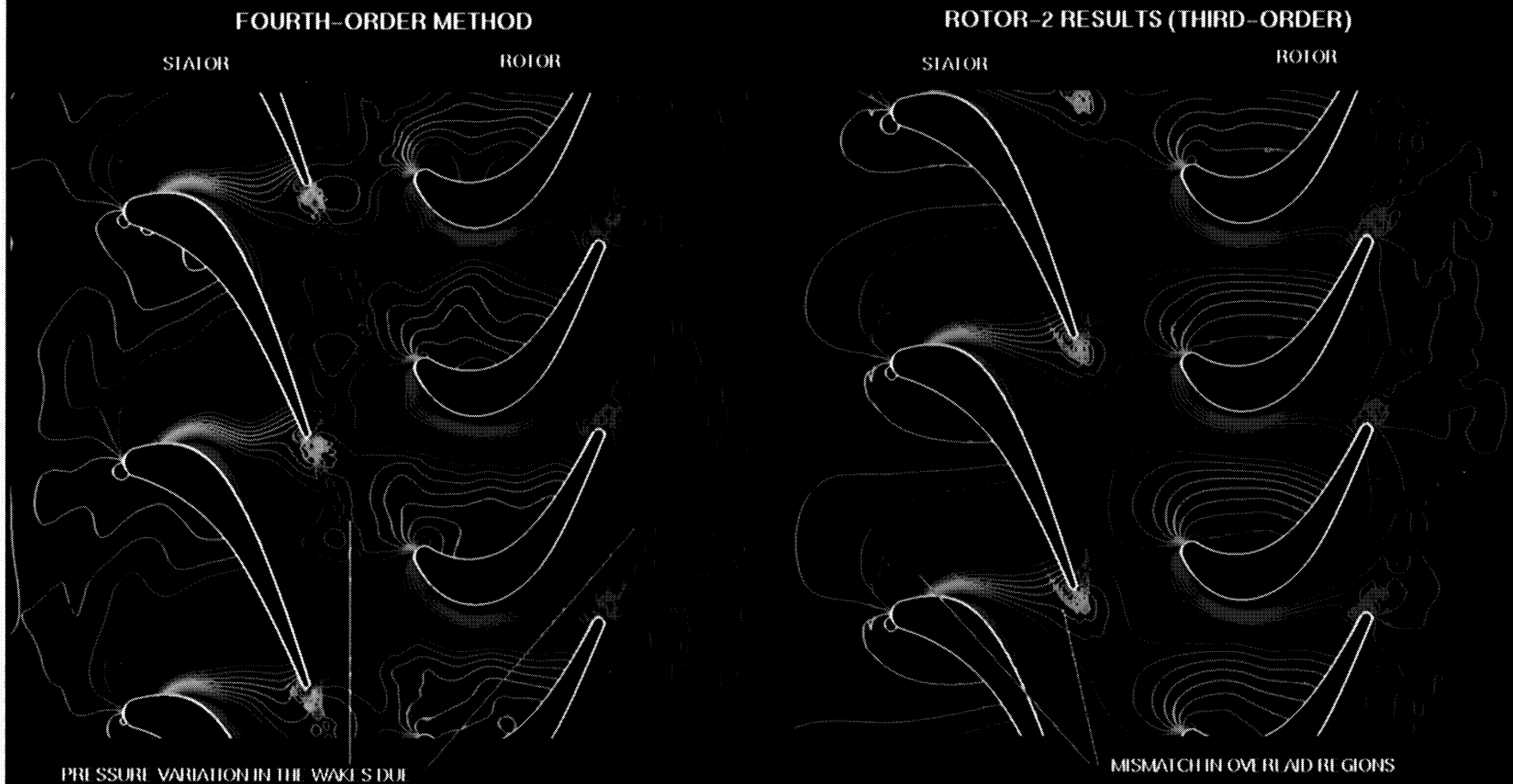

INSTANTANEOUS PRESSURE CONTOURS

(IDENTICAL GRIDS FOR BOTH CASES SHOWN ABOVE)

A COMPARISION BETWEEN THE PRESENT RESULTS AND THOSE OBTAINED BY ROTOR-2 SHOWS THAT THE NEW METHOD IS CAPABLE OF RESOLVING MORE FLOWFIELD DETAILS, SUCH AS THE PRESSURE VARIATION IN THE WAKES. THE ERRORS ASSOCIATED WITH THE ZONAL BOUNDARIES ARE ALSO REDUCED.

FIG. 1 COMPARISIONS OF INSTANTANEOUS PRESSURE CONTOURS

APPENDIX

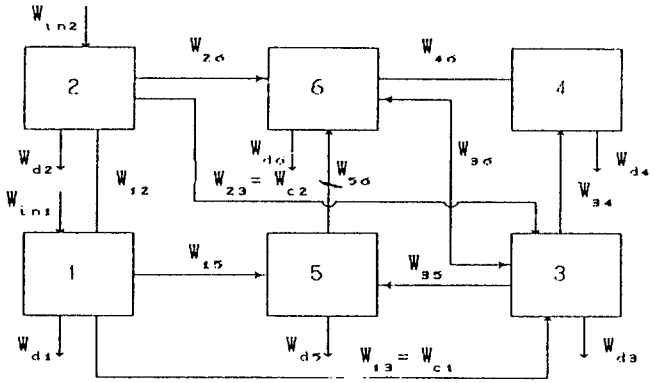

Fig.1 General acoustical model of gear mechanism

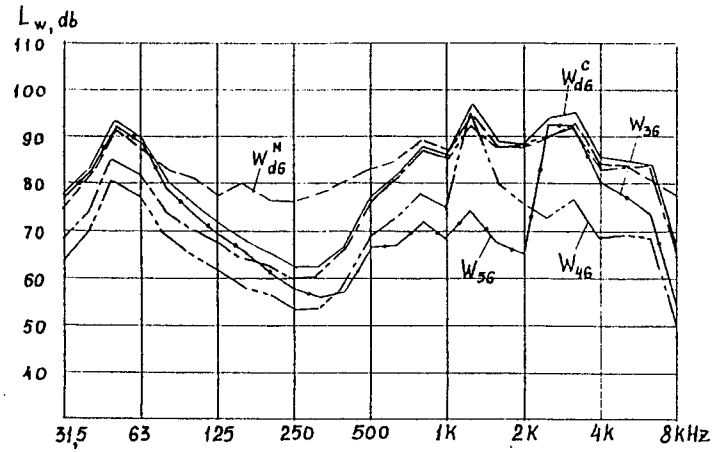

Fig.2 Third octave spectrums of acoustical power of shuttle loading mechanism of multiopening weaving machine NTM-2R

NOISE-93
St. Petersburg, Russia
May 31 - June 3, 1993

COMPUTATIONAL ANALYSIS OF TONAL ACOUSTICS ARISING FROM ROTOR-STATOR INTERACTION IN TURBOMACHINES

Akil A. Rangwalla
MCAT Institute, NASA Ames Research Center, Moffett Field, CA
and
Man Mohan Rai
Senior Scientist, Fluid Dynamics Division
NASA Langley Research Center, Hampton, Virginia

ABSTRACT

Considerable progress has been made in recent years in computing unsteady flows that arise from rotor-stator interaction in turbomachines. These codes have been developed and used successfully to predict the time averaged and unsteady pressure loadings on turbomachinery airfoil surfaces. In this study, the unsteady, thin-layer, Navier-Stokes equations are solved for a rotor-stator configuration of an axial turbine. The focus is on the plurality of spinning modes that are present in such an interaction. The propagation of these modes in the upstream and downstream regions is analyzed and compared with numerical results. It was found that the numerically calculated tonal acoustics could be influenced by the type of numerical boundary conditions employed at the inlet and exit of the computational domain and the grid spacing in the upstream and downstream regions. Results such as the spectra of turbine tones and their far field behavior are presented. The "mode-content" for different harmonics of blade-passage frequency is shown to conform with that predicted by a kinematical analysis.

INTRODUCTION

Both two- and three-dimensional codes have been developed in recent years to compute the unsteady flow in turbomachinery. A two-dimensional calculation of rotor-stator interaction for an axial turbine was presented in [1]. The airfoil geometry and flow conditions were the same as those used in the experiments presented in [2]. More recently, the full three-dimensional flow fields for the same turbine were computed. (See [3] and [4]). The hub, outer casing, and the rotor tip clearance were all included in these calculations. In these computations, the thin-layer Navier-Stokes equations were solved in a time-accurate manner using an implicit, upwind-biased, third-order accurate method. The ability of these codes to predict near field flow quantities such as the time-averaged pressure distributions on airfoil surfaces and the pressure amplitudes and phase on the surface of the airfoils was demonstrated. More recently, these computer programs have also been used in the design process of turbomachines (see [5]). The present work is focussed on investigating the ability of these codes to predict, "correctly", the tonal acoustics in the flow field due to unsteady rotor-stator interactions.

An axial flow turbine (or compressor) produces rotating pressure patterns called spinning modes that may propagate in a spiral path. In two dimensions, these spinning modes propagate at a non-zero angle to the axial direction. For any particular harmonic of blade passing frequency, the interaction field can produce an infinite number of spinning modes, rotating at different speeds. Some of these modes propagate whereas others decay. The modes that are possible for some multiple of blade passing frequency depend upon the number of stator and rotor airfoils. The numerical study of tonal acoustics involves the study of the flow field in the upstream and downstream regions of the interacting rotor and stator airfoils. This raises the issue of the numerical boundary conditions employed at the computational inlet and exit boundaries and the grid spacing used in the upstream and downstream regions. Traditionally, the boundary conditions employed have been reflective. Reflective boundary conditions have been used because they provide greater control on turbine operating conditions such as mass flow and pressure ratio. However, reflective boundary conditions are generally inadequate for the study of tonal acoustics since they reflect the propagating modes back into the computational domain. To overcome this problem, two approaches are used here. The first approach is to use reflective boundary conditions but with a sufficiently long computational domain upstream and downstream of the rotor-stator airfoils. The estimated maximum of the wavelengths of the propagating modes is then used to determine grid spacings at the far upstream and downstream regions so that the propagating modes are dissipated numerically near the boundaries. An acoustic analysis is used to determine the wavelengths of the propagating modes. For methodology and details, see [6], [7] and [8]. This approach will be referred to as the "long-grid" approach. The second approach is to use a short grid but with nonreflective boundary conditions which provided some measure of control over the turbine operating conditions. These boundary conditions are based on

the linear behavior of the flow in the far field. Two types of nonreflective boundary conditions are tested. The first is a differential one-dimensional boundary condition derived from the far field acoustical behavior of the flow and similar to that developed by Bayliss and Turkel ([9], [10] and [11]). The second was an approximate two dimensional unsteady boundary condition developed in [12]. This second approach (using different nonreflective boundary conditions) will be denoted the "short-grid" approach. For the purpose of comparison, short-grid calculations with reflective boundary conditions are also performed.

This study focusses on an examination of the modes present in a rotor-stator interaction for a 3-stator/4-rotor case using a Navier-Stokes solution procedure. Results in the form of turbine tone spectra and axial variation of amplitudes of some modes are presented.

KINEMATICAL ANALYSIS OF INTERACTION TONE NOISE

Reflective boundary conditions, such as a fixed exit static pressure condition, can be made to behave essentially as nonreflective boundary conditions with the use of appropriate grids in the far field region. When the grid cell sizes in the far-field region are of the order of the wavelength of the mode to be attenuated, the energy associated with that mode decays rapidly because of numerical dissipation. Hence, in order to attenuate reflections at the computational boundaries when reflective boundary conditions are used, an estimate of the maximum wavelength in the pressure field is required. Therefore a kinematical analysis of the Fourier modes was carried out. This analysis, when coupled with a linearized analysis of the flow gives important information about the relative magnitudes (of the different Fourier modes) as a function of distance. The method was first used in [6] for the analysis of a single stage and can be generalized for multiple stages. The assumption made here is that the tone generating mechanisms occur at multiples of blade passing frequency. It should be noted that contributions from wake shedding and other aerodynamic noise sources are ignored. The computed results seem to indicate that these secondary contributions are small for the geometry and flow conditions chosen.

The following analysis is limited to two-dimensional flow but can be extended to three dimensions in a straightforward fashion. Consider a single-stage turbine, where S is the number of stator airfoils and R the number of rotor airfoils. The composite pitch is the transverse distance over which the flow is periodic and is denoted by l. The distance between the stator airfoils is l/S and the distance between rotor airfoils is l/R. The velocity of the rotor is denoted by V_R. The pressure at any axial plane in the flow field, is assumed to be periodic in time with period equal to the minimum time required for the rotor-stator geometry to repeat. In the case of a single-stage configuration with identical, equispaced rotor airfoils, the period in a stationary frame of reference is given by $l/|V_R|R$. This is also known as the blade passing time. The pressure variation in any particular axial plane is given by

$$p(y,t) = \sum_{n=0}^{\infty} \sum_{m=-\infty}^{\infty} a_{mn} cos\left(\frac{2\pi}{l}(my - nR|V_R|t) + \phi_{mn}\right) \tag{1}$$

where n is the harmonic of blade passing frequency and m corresponds to the spatial harmonic in y. Assuming that every stator airfoil in the stator row is equally spaced, the pressure variation is assumed to satisfy the shift condition, which states that $p(y,t) = p(y - \frac{l}{S}, t - \frac{l}{S|V_R|})$ which is valid only when frequencies that are non-commensurate with the blade passing frequencies are absent. This then yields

$$m = nR(sgn(V_R)) \pm kS \tag{2}$$

where $k = \ldots, -1, 0, 1, \ldots$ is the spatial harmonic of the disturbance produced by the stators.

Propagating Modes

Analytical solutions representing the unsteady flow in the far field can also be derived, as given in [8]. It is assumed that in the far upstream and downstream regions, the unsteady flow is a linear perturbation of a steady uniform flow. (The underlying steady uniform flow in the upstream region is different from that in the downstream region). A linearized solution of the pressure field indicates that a Fourier mode propagates, if

$$\left| \frac{nR}{m} \frac{M_R}{\sqrt{1 - M_x^2}} + \frac{M_y}{\sqrt{1 - M_x^2}} \right| > 1 \tag{3}$$

where M_R is $\frac{|V_R|}{c}$, M_x is the axial Mach number of the underlying flow and M_y is the transverse Mach number of the underlying flow. The axial wavelength of the propagating mode is denoted by λ_x and is given by

$$\lambda_x = \frac{l(1 - M_x^2)}{M_x(nRM_R + M_y m) \pm sgn(V_R)\sqrt{(nRM_R + M_y m)^2 - (1 - M_x^2)m^2}} \tag{4}$$

where m is given by Eq. (2). For very low values of axial and transverse Mach numbers, M_x, and M_y respectively, the maximum wavelength λ_x can be approximated by substituting 0 for M_x and M_y in Eq. (4). For low values of M_R, it can be seen that for the lower harmonics,

$$[\lambda_x]_{max} = \frac{l}{nRM_R} \tag{5}$$

For a 3-stator/4-rotor case that is presented here, $[\lambda_x]_{max} = l/(3RM_R)$ since the fundamental and the first harmonic do not propagate under the present assumptions of $M_x, M_R \ll 1$. When a long grid is used to dissipate the propagating modes in the far field region, the grid spacings near the exit and inlet boundaries are chosen to be about $[\lambda_x]_{max}/2$. It should be noted that there is a possibility of large axial wave lengths when $nRM_R \approx \sqrt{(1 - M_x^2)}m$, but this would occur only for higher harmonics under the present assumptions of low Mach numbers.

Decaying Modes

A fourier mode will decay with increasing axial distance from the rotor-stator pair if the inequality sign in Eq. (3) is reversed. The amplitude of the mode would vary as

$$a_{mn} \propto e^{\pm d_{mn} x} \tag{6}$$

where

$$d_{mn}^2 = \left(\frac{2\pi}{l}\frac{1}{1 - M_x^2}\right)^2 \left\{(1 - M_x^2)(m)^2 - \left[nRM_R + mM_y\right]^2\right\} \tag{7}$$

A decaying mode decays exponentially. It is understood that for $x < 0$ the positive sign in Eq. (6) is used and for $x > 0$ the negative sign is used. The variation of the natural logarithm of the amplitude ($\log(a_{mn})$) is linear with slope $\pm d_{mn}$.

GEOMETRY AND GRID SYSTEM

The airfoil geometry used is that given in [2]. The two-dimensional computations of this study were performed using the experimental airfoil cross-sections at midspan. These cross-sections, along with a schematic of the computational grid are shown in Figure 1. A system of patched and overlaid grids is used to discretize the flow region of interest. The inner grids are O-grids that were generated using an elliptic grid generator. The outer H-grids were generated algebraically. The experiment consisted of 22 stator airfoils and 28 rotor airfoils. To model the experimental setup the flow over at least 25 airfoils (11 stator airfoils and 14 rotor airfoils) would have to be calculated. This would require excessive computational resources. It was therefore decided to solve a smaller problem by using rescaling strategies as shown in [13] in order to reduce the airfoil count. The number of stator airfoils was changed from 22 to 21 and the size of each individual stator airfoil was enlarged by a factor of 22/21. This rescaling allows a 3-stator/4-rotor computation wherein periodicity is imposed on the flow over 3 stator airfoils and 4 rotor airfoils. Changing the airfoil count does change the nature of the tonal acoustics in the flow field because the mode content of the propagating modes depends upon the airfoil count as indicated by Eqs. (2-7). However, since the objective of this preliminary investigation is to evaluate the capability of rotor-stator interaction codes in calculating tonal acoustics, the rescaled rotor-stator geometry was used. It should be mentioned that Figure 1 shows only a schematic of the grid. The actual number of grid points is much larger and the spacing between the grid points is much smaller. More details about the grid system can be found in [13].

NUMERICAL METHOD

The unsteady, thin-layer, Navier-Stokes equations are solved using an upwind-biased finite-difference algorithm. The kinematic viscosity was calculated using Sutherland's law and the turbulent eddy viscosity was calculated using the Baldwin-Lomax model. The method is third-order-accurate in space and second order-accurate in time. At each time step, several Newton iterations are performed, so that the fully implicit finite-difference equations are solved. Additional details regarding the scheme can be found in [13].

BOUNDARY CONDITIONS

The boundary conditions required when using multiple zones can be broadly classified into two types. The first type consists of the zonal conditions which are implemented at the interfaces of the computational grids and the second type consists of the natural boundary conditions imposed on the surface and the outer boundaries of the computational grid. The treatment of the zonal boundaries can be found in [11]. The natural boundary conditions used in this study are discussed below.

Airfoil Surface Boundary

The boundary conditions on the airfoil surfaces are the "no-slip" condition and adiabatic wall conditions. It should be noted that in the case of the rotor airfoil, "no-slip" implies zero relative velocity at the surface of the airfoil. In addition to the "no-slip" condition, the derivative of pressure in the direction normal to the wall surface is set to zero.

Exit Boundary

One reflective and two radiative boundary conditions were studied. For the reflective boundary condition (see e.g. [13]) the exit pressure was specified and three quantities are extrapolated from the interior. The three quantities are the Riemann variable $R_1 = u + 2c/(\gamma - 1)$, the entropy $S = p/\rho^\gamma$ and v the transverse velocity. This type of boundary condition reflects the pressure waves that reach the boundary back into the system. Two types of radiating boundary conditions were also implemented. The first was a one-dimensional boundary condition formulated by Bayliss and Turkel ([11] and also [15]). It is assumed that at the downstream boundary, the flow is linear. Two-dimensional boundary conditions as presented in [12] were also implemented. As in the previous boundary condition, the flow at the exit is assumed to have small perturbations and hence linearizable about an underlying mean flow. Implementation of this boundary condition requires a knowledge of the underlying exit flow variables, ρ_∞, u_∞, v_∞, and p_∞. The first three quantities are time lagged whereas the exit pressure, p_∞, is kept constant.

Inlet Boundary

One reflective and two radiative boundary conditions were also studied for the inlet. The first was the reflective boundary condition procedure wherein three quantities have to be specified. The three chosen are the Riemann invariant $R_1 = u + 2c/(\gamma - 1) = u_{(-\infty)} + 2c_{(-\infty)}/(\gamma - 1)$ the total pressure $p_{total} = p_{(-\infty)}(1 + (\gamma - 1/2)M^2_{(-\infty)})^{\frac{\gamma}{\gamma - 1}}$ and the inlet flow angle, which in this case is equivalent to $v_{inlet} = 0$. The fourth quantity needed to update the points on this boundary

is also a Riemann invariant but is extrapolated from the interior and is given by $\partial R_2/\partial x = 0$ where $R_2 = u - 2c/(\gamma - 1)$. In the above equations, the quantities u and v are the velocities in the x and y directions, p is the pressure and c is the local speed of sound. Specifying the total pressure at the inlet results in the boundary condition being reflective.

A nonreflective or radiative one-dimensional boundary condition was also implemented. As in the case of the exit boundary, it is assumed that at the upstream boundary the flow is linear, that is, the unsteadiness can be considered a linear perturbation to a steady flow. Two-dimensional inlet boundary conditions were also implemented.

Periodic Upper And Lower Boundaries

The computations reported in this study assume that the flow is spatially periodic in the y direction. The spatial interval of periodicity depends upon the airfoil count. (For example, in the 3-stator/4-rotor case, periodicity is imposed over every 3 stator airfoils and 4 rotor airfoils.) Further details can be found in [1].

RESULTS

In this section, some results obtained for the 3-stator/4-rotor configuration will be presented. In particular, a comparison between the long-grid and short-grid computation with reflective boundary conditions and nonreflective boundary conditions will be made. In addition, the spectrum of the turbine tones and the variation of the amplitudes of the different modes in the far field will be presented.

The dependent variables are nondimensionalized with respect to the far upstream pressure ($p_{(-\infty)}$) and density ($\rho_{(-\infty)}$). The free stream velocity is axial ($v_{(-\infty)} = 0$) and $M_{(-\infty)} = .07$ is the inlet Mach number. The pressure ratio across the turbine ($p_{static_{exit}}/p_{total_{inlet}}$) is 0.963. The rotor velocity was set to match the experimental flow coefficient (ratio of average inlet velocity to rotor speed) of 0.78 as given in [2]. The Reynolds number is 100,000/in. The calculations were performed at a constant time-step value of about 0.16 (this translates into 500 time steps for the rotor to move through a distance equal to the distance between two successive rotor airfoils).

Airfoil Surface Pressure Amplitudes

Comparisons between long and short grid computations for different cases have been made and reported in [15]. In particular, it was found that for this turbine, the predicted time-averaged surface pressures agreed well with the experimental data whereas use of nonreflective boundary conditions and/or a long grid approach did improve the predictions in the pressure amplitudes.

Besides the pressure amplitudes, phase information can also be obtained. The phase of the low pressure peak on the stator suction surface (see [13] for details) for the 3-stator/4-rotor case did not depend on the type of grid or the boundary conditions. The numerical results compared well with experimental data presented in [2] and were similar to those reported in [13].

Far Field Linear Behavior

The spectrum of turbine tones obtained from the computations is presented in this section. Recall that the Fourier modes predicted by the kinematical analysis are denoted by a_{mn} (Eq. 1) where m and n are related as given by Eq. (2). The values of a_{mn} can be obtained by performing a Fourier decomposition of the pressure variation upstream and downstream of the turbine. The upstream results were calculated at two chord-lengths upstream of the leading edge of the stator airfoils and the downstream results were calculated at two chord-lengths downstream of the trailing edge of the rotor airfoils. Figures 2a and 2b show the contribution of the axially aligned planar waves ($m = 0$) for the 3-stator/4-rotor case. The x axis corresponds to harmonics of blade passing frequency and the y axis corresponds to the computed coefficients a_{mn}. For the planar case, ($m = 0$), Eq. (5) predicts the existence of only the $n = 3, 6, 9, \ldots$ harmonics of blade passing frequency. Figure 2a shows the contribution of these planar waves upstream of the stator. Figure 2b shows the contribution of the axially aligned planar waves downstream of the rotor. Since the pressure variations downstream of the rotor are measured in the rotor frame of reference, for the $m = 0$ modes, the kinematical analysis predicts the existence of only the $n = 4, 8, 12, \ldots$ harmonics of blade passing frequency. Similarly, numerical data can also be obtained for $m \neq 0$ modes upstream and downstream of the turbine.

The computations can also be used to study the propagation or decay of the various modes. To do this, either a long grid has to be used and the amplitudes of each mode calculated in the region of the grid where the solution has not suffered from numerical dissipation (due to grid coarseness) or a short grid with nonreflective boundary conditions should be used. A study of the numerical propagation or decay of the different modes has the advantage of determining the grid spacing required in the far-field to maintain a propagating mode or to accurately capture the decay rate of a decaying mode. Additionally, the effect of boundary conditions on the different modes can be assessed.

Comparisons between the theoretical axial wavelengths and those obtained numerically are shown in Tables 1 and 2. Table 1 shows comparisons upstream of the rotor-stator pair. In general, the results are good. The differences are less than the maximum grid spacing in the region where the wavelengths were measured. Table 2 shows a similar comparison downstream of the rotor-stator pair. The numerical results are generally in fair agreement with the theoretical predictions for all (m, n) modes where $m \leq 0$. The differences are of the same order as the maximum grid spacing in the region where the wavelengths were measured. However, the calculated wavelengths of the (m, n) modes where $m > 0$ do not agree well with theoretical predictions. It should be recalled that the theoretical prediction of axial wavelengths (Eq. 4) was obtained under the assumption of a uniform mean flow. However, downstream of the rotor-stator pair, the underlying mean flow is not uniform due to the wakes of the airfoils. It is believed that this nonuniformity in the mean flow is the main reason for the discrepancy between the numerical results and theoretical predictions.

One objective of the present study is to see if nonreflective boundary conditions can be used along with a short grid to predict the tonal acoustics present in rotor-stator interactions. Figures 3a-b show the comparison of short and long grid

calculations with the approximate two-dimensional non-reflective boundary conditions developed in [12]. Comparison with the reflective boundary conditions (Figs. 4a-b) clearly indicates the necessity of non-reflective boundary conditions.

The amplitudes of the decaying modes vary exponentially in the upstream and downstream directions (Eq. 6). The rate of decay depends upon the underlying mean flow and the temporal and spatial frequencies of the mode as given in Eq. (7). (It should be recalled that Eq. (7) is derived under the assumption of linear perturbations to a steady uniform mean flow.) The axial and transverse Mach numbers of the underlying mean flow upstream and downstream of the turbine is obtained from the numerical solutions. The non-dimensional velocity of the rotor airfoils (V_R) is 0.1051282. The quantities M_x, M_y and M_R in Eq. (7) can be evaluated from U_x, U_y, V_R and the sonic velocity of the underlying mean flow.

Figures 5a-b show the axial variation of the amplitudes of some decaying modes upstream and downstream of the rotor-stator pair. It should be noted that Eqs. (6) and (7) yield only the rate of decay and not the amplitude level. Hence in Figs. 5a-b, only the slopes of the curves are of interest. The behavior of these modes upstream of the rotor-stator pair is in excellent agreement with the linear theory in the region where the grid is sufficiently fine (Fig. 5a). In the far upstream region, the numerical solution deviates from the theoretical exponential decay because of the very coarse grid in this region. Downstream of the rotor-stator pair, a difference between the numerical results and the linear theory is seen (Fig. 5b). The axial variation of the natural logarithm of amplitude of the $(-1, 1)$ mode ($\log a_{-1,1}$) is shown in Figure 5b. Even though the overall decay matches that of the theoretical exponential decay, the numerical variation of the amplitude is not a "pure" exponential. Rather, the axial variation of the computed amplitude is exponential as well as oscillatory in nature. This behavior was observed for all (l, k) modes, where $l < 0$. In contrast, all (l, k) modes with $l > 0$ showed exponential decay where the decay rate did not match the theoretical value. It should be recalled that one of the assumptions underlying the theoretical results is a uniform mean flow. However, downstream of the rotor-stator pair, the underlying mean flow does deviate from a uniform flow because of the wakes of the rotor airfoils. This deviation is much more than the deviation upstream of the rotor-stator pair due to potential effects. It is believed that the nonuniformity in the mean flow is the main reason for the discrepancy between the numerical results and theory.

SUMMARY

This study focuses on the numerical computation of tones in rotor-stator interactions. The numerical predictions are obtained by solving the thin-layer Navier-Stokes equations on a system of patched grids. The mode content of interaction tone noise is obtained for a particular airfoil count and is shown to conform with a kinematical analysis of the flow. In addition, the propagation characteristics of different modes are compared with the predictions of linear theory. The effects of both reflective and nonreflective boundary conditions on the calculated flow field were assessed. It was found that for the short-grid calculations, nonreflective boundary conditions had to be used in order to predict the tonal acoustics in the flow field. Use of nonreflective boundary conditions becomes more important for those cases where there is a high energy content in the propagating modes. It was also shown that reflective boundary conditions can be made to behave essentially as nonreflective boundary conditions with the use of appropriate long grids in the upstream and downstream regions. The long grid approach in conjunction with an increasing grid cell sizes in the far upstream and downstream regions results in numerical dissipation of propagating modes, thus avoiding the problems due to reflections at the computational boundaries.

ACKNOWLEDGEMENT

This study was partially supported by NASA Marshall Space Flight Center. Some of the computing resources were provided by the Numerical Aerodynamic Simulation (NAS) program. The authors would like to thank Dr. R. P. Dring of United Technologies Research Center for providing the turbine airfoil geometries used in this investigation.

REFERENCES

(1) Rai, M. M. 1987 Navier - Stokes simulations of rotor-stator interaction using patched and overlaid grids. *AIAA Journal of Propulsion and Power*, **3**, 387-396.

(2) Dring, R. P., Joslyn, H. D., Hardin, L. W. and Wagner, J. H. 1982 Turbine rotor-stator interaction. *Journal of Engineering for Power*, **104**, 729-742.

(3) Rai, M. M. 1989 Three-dimensional Navier-Stokes simulations of turbine rotor stator interaction; Part 1 & 2. *AIAA Journal of Propulsion and Power*, **5**, 305-319.

(4) Madavan, N. K., Rai, M. M. and GAVALI, S. 1989 Grid refinement studies of turbine rotor-stator interaction. *AIAA* Paper No. 89-0325.

(5) Rangwalla, A. A., Madavan, N. K. and Johnson, P. D. 1992 Application of an unsteady Navier-Stokes solver to transonic turbine design. *AIAA Journal of Propulsion and Power*, **8**, 1079-1086.

(6) Tyler, J. M. and Sofrin, T. G. 1970 Axial flow compressor noise studies. *SAE Transactions*, **70**, 309-332.

(7) Goldstein, M. E. 1971 Aeroacoustics. *NASA* SP-346.

(8) Verdon, J. M. 1989 The unsteady flow in the far field of an isolated blade row. *Journal of Fluids and Structures*, **3**, 123-149.

(9) Bayliss, A. and Turkel, E. 1980 Radiation boundary conditions for wave-like equations. *Comm. Pure Appl. Math.*, **33**, 707-725.

(10) Bayliss, A. and Turkel, E. 1982a Far field boundary conditions for compressible flows. *Journal of Comp. Physics*, **48**, 182-199.

(11) Bayliss, A. and Turkel, E. 1982b Outflow boundary conditions for fluid dynamics. *SIAM J. Sci. Stat. Comput.*, **3**, 250-259.

(12) Giles, M. 1988 Non-reflecting boundary conditions for the Euler equations. *CFDL-TR-88-1*, MIT Computational Fluid Dynamics Laboratory.

(13) Rai, M. M. and Madavan, N. K. 1990 Multi-airfoil Navier-Stokes simulations of turbine rotor-stator interaction. *ASME Journal of Turbomachinery*, 112, 377-384.

(14) Rai, M. M. 1986 An implicit conservative zonal boundary scheme for Euler equation calculations. *Computers and Fluids*, 14, 99-131.

(15) Rangwalla, A. A. and Rai, M. M. 1990 A kinematical/numerical analysis of rotor-stator interaction noise. *AIAA* Paper No. 90-0281.

Table 1 Axial wavelengths of some propagating modes (upstream); 3-stator/4-rotor case. (Theory in parentheses).

m	-2	-1	0	1	2
n=1		decaying			decaying
n=2	decaying			decaying	
n=3			20.54(21.11)		
n=4		20.81(21.63)			decaying
n=5	decaying			14.96(15.09)	
n=6			10.49(10.55)		
n=7		9.46(9.81)			14.15(14.48)
n=8	10.57(10.82)			8.11(8.41)	
n=9			7.03(7.04)		
n=10		6.35(6.58)			7.16(7.55)

Table 2. Axial wavelengths of some propagating modes (downstream); 3-stator/4-rotor case. (Theory in parentheses).

m	-2	-1	0	1	2
n=1		decaying			
n=2	decaying				decaying
n=3				decaying	
n=4			23.51(20.96)		
n=5		23.78(26.91)			
n=6	decaying				decaying
n=7				18.38(13.39)	
n=8			11.65(10.48)		
n=9		10.81(10.47)			
n=10	11.89(13.46)				20.81(11.12)

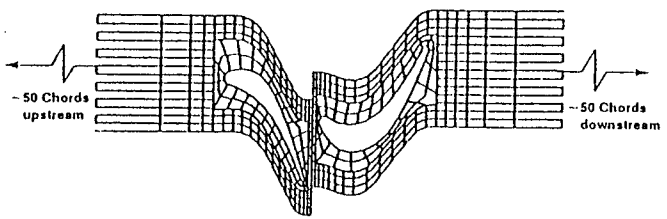

Figure 1. Rotor-stator geometry and grid.

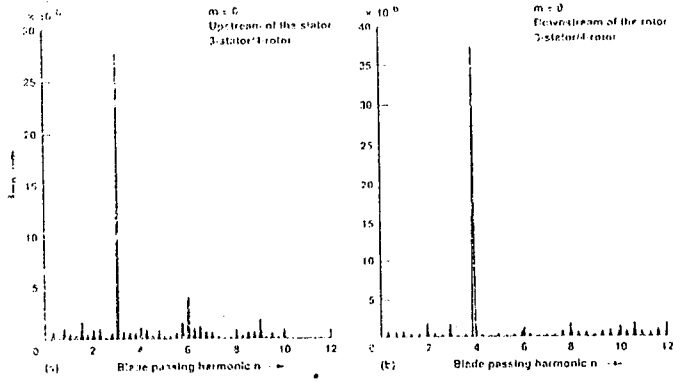

Figure 2. Spectrum of the (a) $m = 0$ mode upstream of the stator and (b) the $m = 0$ mode downstream of the rotor for the 3-stator/4-rotor case.

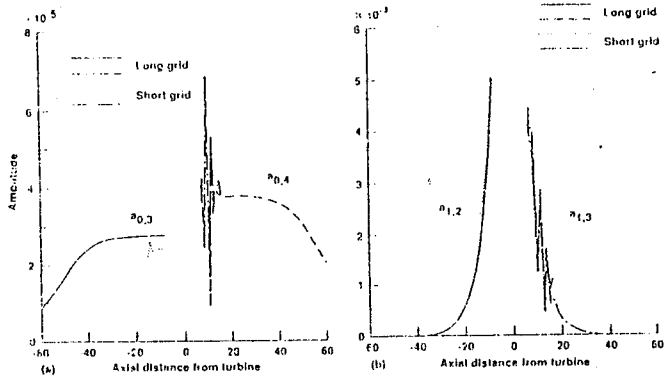

Figure 3. Comparison between a long grid solution and a short grid solution with non-reflective boundary conditions for the (a) (0, 3) mode upstream and (0, 4) mode downstream of the rotor-stator pair and the (b) (1, 2) mode upstream and (1, 3) mode downstream of the rotor-stator pair.

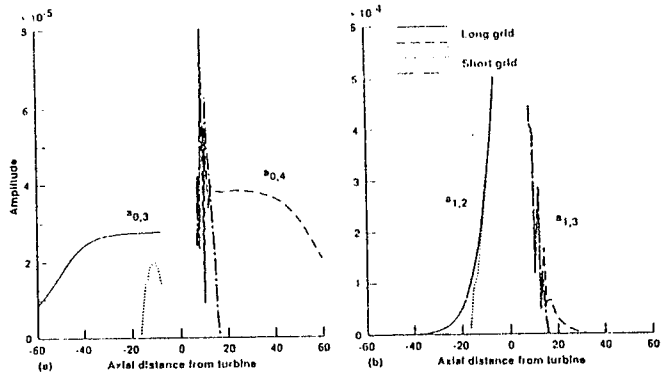

Figure 4. Comparison between a long grid solution and a short grid solution with reflective boundary conditions for the (a) (0, 3) mode upstream and (0, 4) mode downstream of the rotor-stator pair and the (b) (1, 2) mode upstream and (1, 3) mode downstream of the rotor-stator pair.

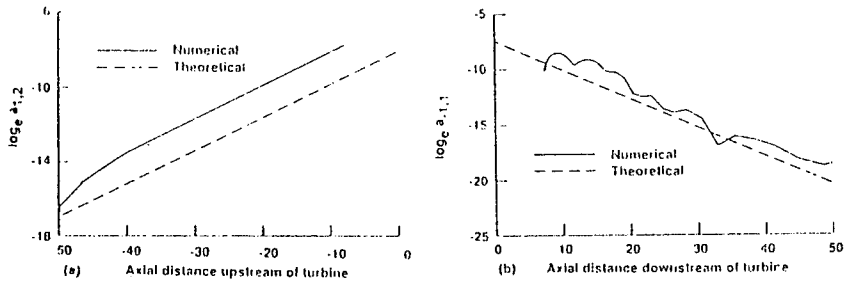

Figure 5. Comparison between numerical and theoretical decay rates (a) mode (1, 2) upstream and (b) mode (−1, 1) downstream.

NOISE-93
St. Petersburg, Russia
May 31 - June 3, 1993

TURBOCHARGER NOISE, GENERATING MECHANISMS AND CONTROL

Sunil N. Sabay
Product Engineering
Garrett Automotive Group
Torrance, California 90505
U.S.A.

Denis Thouvenin
Engineering Department
Garrett, S.A.
Thaon-les-Vosges
France

ABSTRACT

Turbochargers, with maximum running speed in excess of 200,000 rpm, are perhaps the fastest running turbomachinery in today's Automotive industry. Turbocharger noise problem came into prominence with the application of turbochargers on passenger cars in early 1970. During the early period of its application, a "pure tone" noise synchronous with the turbocharger speed, was the dominant objectionable noise and it was controlled by reducing the imbalance level. Since then, additional types of turbocharger noise, excited by mechanical vibration and air flow, have been encountered . The trend towards lighter and more compact vehicles with reduced engine space has increased vehicle's response to turbocharger generated vibration and pressure pulsations that result in vehicle noise. This presents an ever-increasing challenge to the turbocharger manufacturers for producing quiet turbochargers. This paper presents a brief description of the different types of turbocharger noise, their generating mechanisms and control. In most cases, the noise reduction is achieved by design improvement and better control of manufacturing process. This consists of changing the rotor-bearing system design, improving the balance process to correct extremely small amount of imbalance and tightening the casting and machining tolerances for more symmetrical compressor and turbine wheels.

INTRODUCTION

Turbochargers are very high speed turbomachinery, used primarily on automotive vehicles to increase the power output of a given size of engine. Till the end of last decade, turbocharger noise was addressed on a "fire fighting" basis. A prior assessment of potential noise problem was not done during the design and development phase which resulted in high cost for noise control . This has now started to change and potential noise problems are being addressed from the start of design. This paper will describe the various noise generating mechanisms and the steps taken during the development of a new turbocharger to control the noise generation. The development of this turbocharger is nearing completion and the information presented is based on development testing. The next step in the cost effective noise control is for the turbocharger manufacturer to provide turbocharger related input to the vehicle manufacturer at the start of a new engine/vehicle program and stay involved till the design is complete.

Journal of Fluids and Structures (1993) **7**, 611–637

A NUMERICAL ANALYSIS OF TONAL ACOUSTICS IN ROTOR-STATOR INTERACTIONS

A. A. RANGWALLA
MCAT Institute, NASA Ames Research Center

AND

M. M. RAI
NASA Ames Research Center, Moffett Field, California 94035, U.S.A.

(Received 19 November 1991 and in revised form 21 January 1993)

In this study, the unsteady, thin-layer, Navier-Stokes equations are solved using a system of patched grids for a rotor-stator configuration of an axial turbine. The study focuses on the plurality of spinning modes that are present in such an interaction. The propagation of these modes in the upstream and downstream regions is analysed and compared with numerical results. It was found that the numerically calculated tonal acoustics could be affected by the type of numerical boundary conditions employed at the inlet and exit of the computational boundaries and the grid spacing in the upstream and downstream regions. Results in the form of surface pressure amplitudes and the spectra of turbine tones and their far field behavior are presented. Numerical results and experimental data are compared wherever possible. The "mode-content" for different harmonics of blade-passage frequency is shown to conform with that predicted by a kinematical analysis.

1. INTRODUCTION

THE FLUID FLOW WITHIN A TURBOMACHINE is inherently unsteady. There are several mechanisms that cause the unsteadiness, and some of these are, (a) the relative motion between the rotors and stators (which is also called the inviscid or potential effect), (b) the interaction of the downstream airfoils with the wakes generated by the upstream airfoils, and (c) the shedding of vortices at blunt trailing edges. In general, as the axial gap between the stator and rotor airfoils decreases, the magnitude of the unsteady interactions increases. These interactions can even become strongly coupled. Hence, to study unsteady processes involved within a turbomachine, it may be essential to treat the rotor and stator airfoils as a single system.

Pioneering work in predicting inviscid rotor-stator interaction was conducted by Erdos *et al.* as far back as 1977. However, the subject has only very recently become the focus of increasing attention due to the considerable increase in computational resources. Lewis *et al.* (1987) solved the quasi three-dimensional inviscid equations, and Jorgenson & Chima (1988, 1989) used the explicit Runge–Kutta method to solve the quasi-three-dimensional Euler and thin-layer Navier–Stokes equations. Three-dimensional periodic calculations have also been presented by Koya & Kotake (1985). Gibeling *et al.* (1986) presents results for the flow in a compressor stage obtained using a shearing grid technique. Here, a single grid is used to discretize the flow domain and is allowed to shear in order to allow relative motion between the rotor and stator airfoils. The data from the sheared grid are interpolated onto an undistorted initial grid

0889–9746/93/060611 + 27 $08.00

at regular time intervals so as to limit the cumulative distortion due to grid shear The development of general zonal techniques and robust, accurate algorithms for numerical solution of Euler and Navier-Stokes equations has contributed further to development of rotor-stator interaction codes. Giles (1988a) has calculated t dimensional rotor-stator interactions using the Euler equations. In this work, a nc concept of a "time-inclined" computational plane is used in order to surmo difficulties encountered when the stator-rotor pitch ratios is not a ratio of two sn integers. Rai (1987) presented a two-dimensional calculation of rotor-stator interact for an axial turbine. The airfoil geometry and flow conditions were those given in Dr *et al.* (1982). More recently, Rai (1989) and Madavan *et al.* (1989) computed the fi three-dimensional flow fields for the same case. The hub, outer casing and the rotor clearance were all included in the calculation. Rai (1987, 1989) and Madavan *et* (1989) solved the thin-layer Navier-Stokes equations in a time-accurate manner us an implicit, upwind-biased, third-order accurate method to compute the flow field. T ability of their codes to predict near field flow quantities, such as the time-averag pressure distributions on airfoil surfaces and the pressure amplitudes and phase on surface of the airfoils, was demonstrated. In addition, the two-dimensional codes we used to predict accurately the total pressure defects in wakes. These compu programs have also been recently used in the design process of turbomachir (Rangwalla *et al.* 1992). Rotor-stator interaction codes have also been used to calcul "sensitive" flow quantities such as heat transfer (Rao *et al.* 1992a, b; Griffin McConnaughey 1989) and three-dimensional unsteady hot streak migration (Dorney *al.* 1990). Recently, the codes have also been extended for multiple stage calculatio by Gundy-Burlet *et al.* (1991). More recently, Dorney (1992) performed a rigoro validation of a modified rotor-stator algorithm through comparisons with analytical a linearized unsteady aerodynamic solutions. The present work is focussed on investig ing the ability of rotor–stator codes to predict "correctly" the tonal acoustics in t flow field due to rotor–stator interactions.

An axial flow turbine (or compressor) produces rotating pressure patterns call spinning modes that may propagate in a spiral path. In two dimensions, these spinni modes propagate at a non-zero angle to the axial direction. For any particul harmonic of blade passing frequency, the interaction field can produce an infini number of spinning modes. Each of these modes rotates at a different speed. Some these modes propagate, whereas others decay. The modes that are possible for son multiple of blade passing frequency depends upon the number of stator and rot airfoils. This study focusses on an examination of the modes present in a rotor-stat interaction for both a single-stator/single-rotor and a 3-stator/4-rotor case using Navier-Stokes solution procedure.

The numerical study of tonal acoustics involves the study of the flow field in th upstream and downstream regions of the interacting rotor–stator airfoils. This raise the issue of the numerical boundary conditions employed at the computational inl and exit boundaries and the grid spacing used in the upstream and downstream region Traditionally, the boundary conditions employed have been reflective. Reflectiv boundary conditions have been used because they provide greater control on turbin operating conditions, such as mass flow and pressure ratio. However, reflectiv boundary conditions are generally inadequate for the study of tonal acoustics since the reflect the propagating modes back into the flow field. Rai & Madavan (1990 performed a 1-stator/1-rotor calculation with non-reflective boundary conditions base on Riemann invariants. These non-reflective boundary conditions were the same a those developed by Erdos *et al.* (1977). However it was found that the use of suc

boundary conditions resulted in a loss of control over the mass flow rate through the turbine. To overcome this problem, two approaches were tried. The first approach was to use reflective boundary conditions but with a sufficiently long computational domain upstream and downstream of the rotor–stator airfoils. The estimated maximum of the wavelengths of the propagating modes was then used to determine grid spacings at the far upstream and downstream regions, so that the propagating modes are numerically dissipated near the boundaries. An acoustic analysis based upon the methodology developed by Tyler & Sofrin (1970), Goldstein (1974) and Verdon (1989) is applied to determine the wavelengths of the propagating modes. This approach will be referred to as the "long-grid" approach. The second approach was to use a short grid, but with non-reflective boundary conditions, which provided some measure of control over the turbine operating conditions. These boundary conditions are based on the linear behavior of the flow in the far field. Two types of non-reflective boundary conditions were tested. The first was a differential one-dimensional boundary condition derived from the far field acoustical behavior of the flow and similar to that developed Bayliss & Turkel (1980, 1982a, b). The second was an approximate two-dimensional unsteady boundary condition developed by Giles (1988b). This second approach (using different non-reflective boundary conditions) will be denoted the "short-grid" approach. For the purpose of comparison, short-grid calculations with reflective boundary conditions were also performed.

The computations that have been carried out so far, are for two different configurations: a single-stator/single-rotor case and a three-stator/four-rotor case. Both cases were computed using the long-grid approach as well as the short-grid approach and the corresponding results are compared. Additionally, results in the form of surface pressure amplitudes, the spectra of turbine tines and the axial variation of amplitudes in the near and far field regions of the different modes are presented.

2. KINEMATICAL PREDICTION OF INTERACTION TONE NOISE

Reflective boundary conditions, such as a fixed exit static pressure condition, can be made to behave essentially as a non-reflective boundary condition with the use of appropriate grids in the far field region. When the grid cell sizes in the far-field region are of the order of the wavelength of the mode to be attenuated, the energy associated with that mode decays rapidly because of numerical dissipation. Hence, in order to attenuate reflections at the computational boundaries when reflective boundary conditions are used, an estimate of the maximum wavelength in the pressure field is required. Therefore a kinematical analysis of the Fourier modes was carried out. This analysis, when coupled with a linearized analysis of the flow gives important information about the relative magnitudes (of the different Fourier modes) as a function of distance. The method was first used by Tyler & Sofrin (1970) for the analysis of a single stage and this study is generalized for multiple stages. The single stage results are presented first followed by the results for multiple stages. The assumption made here is that the tone generating mechanisms occur at multiples of blade passing frequency. It should be noted that contributions from wake shedding and other aerodynamic noise sources are ignored. The computed results seem to indicate that these secondary contributions are small for the geometry and flow conditions chosen.

The analysis that follows is limited to two-dimensional flow. However, extension to three dimensions is straightforward. Consider a single-stage turbine as shown in

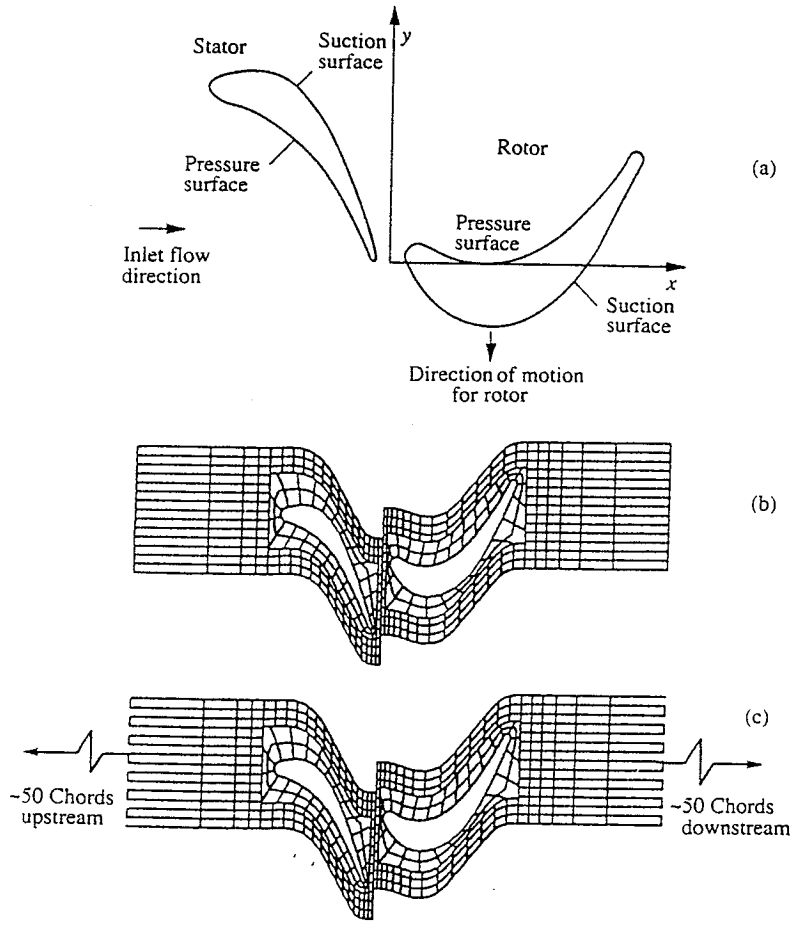

Figure 1. (a) Rotor–stator geometry; (b) short grid; (c) long grid.

Figure 1(a). Let S be the number of sator airfoils and R the number of rotor airfoils The composite pitch is the transverse distance over which the flow is periodic and i denoted by l. Hence, the distance between the stator airfoils is L/S and the distanc between rotor airfoils is l/R. The velocity of the rotor is denoted by V_R. The pressur at any axial plane in the flow field, is assumed to be periodic in time, with period equa to the minimum time required for the rotor-stator geometry to repeat. In the case of a single-stage configuration with identical equispaced rotor airfoils, the period in a stationary frame of reference is given by $l/|V_R|R$. This is also known as the blade passing time. The pressure variation in the axial plane can be written as

$$p(y, t) = \sum_{n=0}^{\infty} p_n(y) \cos\left[2\pi nt \frac{|V_R| R}{l} + \Phi_n(y)\right], \tag{1}$$

where $p_n(y)$ is the amplitude of the nth Fourier component and $\Phi_n(y)$ is the phase. It should be noted that $p_n(y)$ and $\Phi_n(y)$ are periodic functions in y with period equal to the composite pitch l. Using this periodicity in y and appropriate trigonometric identities, ultimately results in

$$p(y, t) = \sum_{n=0}^{\infty} \sum_{m=-\infty}^{\infty} p_{mn}, \tag{2}$$

where

$$p_{mn} = a_{mn} \cos\left[\frac{2\pi}{l}(my - nR\,|V_R|\,t) + \phi_{mn}\right], \tag{3}$$

where n is the harmonic of blade passing frequency and m corresponds to the spatial harmonic in y. The next assumption that is made is crucial to the analysis. Considering that all stator airfoil in the stator row are equally spaced, the pressure variation is assumed to satisfy the shift condition, which states that

$$p(y, t) = p\left(y - \frac{l}{S}, t - \frac{l}{SV_R}\right). \tag{4}$$

It should be noted that both equations (1) and (4) are valid only when frequencies that are non-commensurate with the blade passing frequencies are absent. Substituting equation (4) in equation (2) then yields

$$m = nR\,\mathrm{sgn}(V_R) \pm kS \tag{5}$$

where $k = \ldots, -1, 0, 1, \ldots$ is the spatial harmonic of the disturbance produced by the stators.

2.1 Propagating Mode

Analytical solutions representing the unsteady flow in the far field can also be derived (Verdon 1989). It is assumed that in the far upstream and downstream regions, the unsteady flow is a linear perturbation of a steady uniform flow. (The underlying steady uniform flow in the upstream region is different from that in the downstream region.) A linearized solution of the pressure field (Verdon 1989) indicates that a Fourier mode propagates, if

$$\left|\frac{nR}{m}\frac{M_R}{\sqrt{1 - M_x^2}} + \frac{M_y}{\sqrt{1 - M_x^2}}\right| > 1, \tag{6}$$

where M_R is $|V_R|/c$, M_x is the axial Mach number of the underlying flow and M_y is the transverse Mach number of the underlying flow. The axial wave-number of the propagating mode is

$$k_x = \frac{1}{1 - M_x^2}\left[M_x\frac{\beta}{c} \pm \mathrm{sgn}(V_R)\sqrt{\frac{\beta^2}{c^2} - a^2}\right], \tag{7}$$

where

$$\beta = \frac{2\pi}{l}(nR\,|V_R| + cM_y m), \qquad \alpha = \frac{2\pi m}{l}\sqrt{1 - M_x^2}$$

and c is the sonic velocity in the underlying steady flow. The axial wavelength of the propagating mode is denoted by λ_x and is equal to $2\pi/k_x$. Using equation (7) we get

$$\lambda_x = \frac{l(1 - m_x^2)}{M_x(nRM_R + M_y m) \pm \mathrm{sgn}(V_R)\sqrt{(nRM_R + M_y m)^2 - (1 - M_x^2)m^2}}, \tag{8}$$

where m is given by equation (5). For very low values of axial and transverse Mach

numbers, M_x and M_y, respectively, the maximum wavelength, λ_x, can be approximate by substituting 0 for M_x and M_y in equation (8). For low values of M_R, it can be see that for the lower harmonics,

$$[\lambda_x]_{\max} = \frac{l}{nRM_R}, \tag{9}$$

In the case of a single-stator/single-rotor calculation, all harmonics would have spati modes that would propagate as indicated by equation (6) and hence the maximu possible wavelength at the lower harmonics is

$$[\lambda_x]_{\max} = \frac{l}{M_R}, \tag{10a}$$

whereas, for a 3-stator/4-rotor case,

$$[\lambda_x]_{\max} = \frac{l}{3RM_R}, \tag{10b}$$

since for this case the fundamental and the first harmonic do not propagate under th present assumptions of $M_x, M_R \ll 1$. When a long grid is used to dissipate th propagating modes in the far field region, the grid spacings near the exit and inl boundaries are chosen to be about $[\lambda_x]_{\max}/2$. It should be noted that there is possibility of large axial wavelengths when $nRM_R \approx \sqrt{(1 - M_x^2)}m$, but this would occu for higher harmonics under the present assumptions of low Mach numbers.

2.2. Decaying Mode

A Fourier mode would decay with increasing axial distance from the rotor-stator pair the inequality sign in equation (6) is reversed. The amplitude of the mode would var as

$$a_{mn} \propto e^{\pm d_{mn}x}, \tag{11}$$

where

$$d_{mn}^2 = \left(\frac{2\pi}{l}\frac{1}{1 - M_x^2}\right)^2 \{(1 - M_x^2)(m)^2 - [nRM_R + mM_y]^2\}. \tag{12}$$

A decaying mode decays exponentially. It is understood that for $x < 0$ the positive sig in equation (11) is used and for $x > 0$ the negative sign is used. The variation of th natural logarithm of the amplitude, $\log(a_{mn})$, is linear with slope $\pm d_{mn}$.

2.3. Multiple Stages

The analysis is similar in the case of multiple stages. Let the number of rotor rows be and number of stator rows be s. Denote the number of airfoils in the rotor rows a $R_1, R_2, \ldots, R_r$ and the number of stator airfoils in stator rows as $S_1, S_2, \ldots, S_s$. Th

composite pitch is again denoted by l, so that the distance between the airfoils in rotor row i is l/R_i, and the distance between the airfoils in the stator row i is l/S_i. Define

$$R = \text{Highest common factor } (R_1, R_2, \ldots, R_r)$$

and

$$S = \text{Highest common factors } (S_1, S_2, \ldots, S_s).$$

The stator and rotor rows can be aligned arbitrarily; however, it is assumed that all the rotors have the same velocity, V_R. It is also assumed that in each individual row, the airfoils are identical and equispaced. The minimum time for the rotor-stator geometry to repeat is again equal to $l/|V_R|\,R$. Thus, the pressure variation on any axial plane is given by equation (1), and the shift condition is given by equation (4). R and S can now be considered to be the number of rotor and stator airfoils on an "equivalent" single-stage configuration. The rest of the analysis is similar.

3. GEOMETRY AND GRID SYSTEM

The airfoil geometry used is that given by Dring *et al.* (1982). The two-dimensional computations of this study were performed using the experimental airfoil cross-sections at midspan. These cross-sections are shown in Figure 1(a). A system of patched and overlaid grids is used to discretize the flow region of interest. Figure 1(b) shows a typical system of grids used in this study. The inner grids are O-grids and were generated using an elliptic grid generator. The outer H-grids were generated algebraically. The experiment consisted of 22 stator airfoils and 28 rotor airfoils. To model the experimental set-up the flow over at least 25 airfoils (11 stator airfoils and 14 rotor airfoils) would have to be calculated. This would require excessive computational resources. It was therefore decided to solve a smaller problem by using rescaling strategies adopted by Rai (1987) and Rai & Madavan (1990) in order to reduce the airfoil count.

The tonal acoustics for two different rescalings were computed. In the first case, the number of rotor airfoils was changed from 28 to 22. The size of each individual rotor airfoil was enlarged by a factor of 28/22 such that the pitch-to-chord ratio of the rotor was unchanged. This rescaling results in a turbine which has equal number of stator and rotor airfoils, thus allowing a single-stator/single-rotor calculation. (Flow periodicity is imposed over one stator airfoil and one rotor airfoil.) In the second case, the number of stator airfoils was changed from 22 to 21. The size of each individual stator airfoil was enlarged by a factor 22/21. This rescaling allows a 3-stator/4-rotor computation wherin periodicity is imposed on the flow over three stator airfoils and four rotor airfoils. Changing the airfoil count does change the nature of the tonal acoustics in the flow field because the mode content of the propagating modes depends upon the airfoil count as indicated by equations (5–12). However, the objective of this preliminary investigation is to evaluate the capability of rotor-stator interaction codes to calculate tonal acoustics. Hence a numerical solution of a rescaled rotor–stator geometry can be used to establish numerical boundary condition and grid requirements. Figure 1(b) shows a typical grid for the single-rotor/single-stator calculation. However, if the grid spacing at the upstream and downstream boundaries is chosen to attenuate reflections as described in the previous section, the grid would have to be lengthened as shown in Figure 1(c). It should be noted that both the long and the short grids are identical in the near field region.

3.1. Grid Density

It should be mentioned that Figure 1 only shows a schematic of the grid. The actual number of grid points is much larger and the spacing between the grid points is much smaller. In all the calculations, each inner O-grid had 151 points along the airfoil surfaces and 41 points in the wall normal direction for a total number of 6,191 grid points in each O-grid. Each H-grid had 71 grid points in the y-direction and 90 to 141 grid points in the x-direction (90 points for the short grid case and 141 points for the long grid case). This results in each short H-grid having 6,390 grid points and each long H-grid having 10,011 grid points. The total number of grid points used for the 3-stator/4-rotor short grid computation was $7 \times (6{,}191 + 6{,}390) = 88{,}067$ whereas for the long grid computation, the total number of grid points was $7 \times (6{,}191 + 10{,}011) = 133{,}414$. Rai and Madavan (1990) give more details about the grid system.

4. NUMERICAL METHOD

The unsteady, thin-layer, Navier-Stokes equations are solved using an upwind-biased finite-difference algorithm. The method is third-order-accurate in space and second-order-accurate in time. At each time step, several Newton iterations are performed, so that the fully implicit finite-difference equations are solved. Additional details regarding the scheme can be found in Rai (1987).

5. BOUNDARY CONDITIONS

The boundary conditions required when using multiple zones can be broadly classified into two types. The first type consists of the zonal conditions which are implemented at the interfaces of the computational meshes and the second type consists of the natural boundary conditions imposed on the surface and the outer boundaries of the computational mesh. The treatment of the zonal boundaries can be found in Rai (1986). The natural boundary conditions used in this study are discussed below. In particular radiating boundary conditions for the inlet and exit boundaries are presented.

5.1. Airfoil Surface Boundary

The boundary conditions on the airfoil surfaces are the "no-slip" condition and adiabatic wall conditions. It should be noted that in the case of the rotor airfoil, "no-slip" does not imply zero absolute velocity at the surface of the airfoil, but rather, zero relative velocity. In addition to the "no-slip" condition, the derivative of pressure in the direction normal to the wall surface is set to zero.

5.2. Exit Boundary

Two types of boundary conditions were used at this boundary. The first was a reflective boundary condition where the exit pressure was specified and three quantities are

extrapolated from the interior. The boundary conditions are

$$p_{\text{static}} = \text{constant}, \tag{13a}$$

$$\frac{\partial R_1}{\partial x} = 0, \qquad \frac{\partial S}{\partial x} = 0 \tag{13b, c}$$

and

$$\frac{\partial v}{\partial x} = 0, \tag{13d}$$

where $R_1 = u + 2c/(\gamma - 1)$ is the Riemann variable, $S = p/\rho^\gamma$ is the entropy and v is the transverse velocity. This type of boundary condition reflects the pressure waves that reach the boundary back into the system. Two types of radiating boundary conditions were also implemented. The first was a one-dimensional boundary condition and its formulation (Bayliss & Turkel 1982) is shown below. It is assumed that, at the down-stream boundary, the flow is linear, that is, the unsteadiness can be considered a linear perturbation to a steady flow. This steady flow need not be axial. However, we can always rotate the coordinate system such that the x-axis is aligned with the underlying steady flow. In the rest of the analysis, it is assumed that the coordinates are so aligned. The linearized Euler equations far downstream are given by

$$\frac{\partial}{\partial t}\begin{Bmatrix} \rho' \\ u' \\ v' \\ p' \end{Bmatrix} + \begin{bmatrix} u_e & \rho_e & 0 & 0 \\ 0 & u_e & 0 & \frac{1}{\rho_e} \\ 0 & 0 & u_e & 0 \\ 0 & \rho_e c_e^2 & 0 & u_e \end{bmatrix} \frac{\partial}{\partial x}\begin{Bmatrix} \rho' \\ u' \\ v' \\ p' \end{Bmatrix} + \begin{bmatrix} 0 & 0 & \rho_e & 0 \\ 0 & 0 & 0 & 0 \\ 0 & 0 & 0 & \frac{1}{\rho_e} \\ 0 & 0 & \rho_e c_e^2 & 0 \end{bmatrix} \frac{\partial}{\partial y}\begin{Bmatrix} \rho' \\ u' \\ v' \\ p' \end{Bmatrix} = 0, \tag{14}$$

where u_e, ρ_e and c_e are the underlying steady state velocity, density and speed of sound at the exit, whereas, p', ρ', u' and v' are the perturbations in the pressure, the density, the velocity in the direction of the mean flow, and the velocity normal to the mean flow, respectively. Using the linearized x-momentum, y-momentum and energy equations, we can obtain

$$p'_{tt} - 2u_e p'_{xt} - (c_e^2 - u_e^2)p'_{xx} - c_e^2 p'_{yy} = 0. \tag{15}$$

Introducing the change in variables

$$\xi = \frac{x}{\sqrt{1 - M_e^2}}, \qquad \eta = y$$

and

$$\tau = c_e\sqrt{1 - M_e^2}t + M_e\xi,$$

equation (15) is transformed to

$$p'_{\tau\tau} - p'_{\xi\xi} - p'_{\eta\eta} = 0. \tag{16}$$

Equation (16) admits solutions of the form

$$p' = f(\tau - \xi\cos\theta + \eta\sin\theta), \tag{17}$$

where θ is the angle between the underlying mean flow and the axial direction ($\theta = \tan^{-1}(v_\infty/u_\infty)$; $u_e = \sqrt{u_\infty^2 + v_\infty^2}$). These solutions are planar waves propagating in the axial direction. Since in the present calculation the airfoils extend from $\eta = -\infty$ to $+\infty$ waves of this form are expected to exist. It should be noted that a boundary condition

based on equation (17) will be non-reflective for one-dimensional cases. Equation (17 suggests a differential operator of the form $\mathscr{L} = (\partial/\partial\tau) + \cos\theta(\partial/\partial\xi) - \sin\theta(\partial/\partial\eta$ which annihilates the functional form in equation (17). Hence the radiating boundar condition used is $\mathscr{L}p = 0$. which when transformed into the actual physical non-rotate coordinates give, for $M_\infty \ll 1$,

$$p'_t = \rho_\infty c_\infty (1 + M_{x\infty})(u'_t + u_\infty u'_x). \tag{18}$$

Implementation of equation (18) is done by first setting u'_x equal to zero. This consistent with the zeroth order extrapolation of the velocities at the boundary. Th velocities u and v and the entropy p/ρ^γ are extrapolated from the interior. Th pressure is updated on the exit boundary by using equation (18). In this equation, th terms ρ_∞, u_∞ and v_∞ are obtained by circumferentially averaging ρ, u and v at the ex at the previous time step. The exit sonic speed, c_∞, is evaluated by using $c_\infty = \sqrt{\gamma p_\infty/\rho_\infty}$ where the value of p_∞ is fixed and is equal to the exit pressure value used in th reflective boundary condition procedure.

The boundary condition described above is essentially a one-dimensional boundar condition. Two-dimensional boundary conditions as developed by Giles (1988b) wer also implemented. As in the previous boundary condition, the flow at the exit assumed to have small perturbations and hence be linearizable about an underlyin mean flow. The exit boundary conditions in terms of one-dimensional characteristi variables are

$$\frac{\partial c_4}{\partial t} + \{0 \quad u_\infty \quad 0 \quad v_\infty\} \frac{\partial}{\partial y} \begin{Bmatrix} c_1 \\ c_2 \\ c_3 \\ c_4 \end{Bmatrix} = 0, \tag{19a}$$

$$\frac{\partial}{\partial x} \begin{pmatrix} c_1 \\ c_2 \\ c_3 \end{pmatrix} = 0, \tag{19b}$$

where the transformation between the characteristic variables and the perturbatio variables is given by

$$\begin{Bmatrix} c_1 \\ c_2 \\ c_3 \\ c_4 \end{Bmatrix} = \begin{bmatrix} -c_\infty^2 & 0 & 0 & 1 \\ 0 & 0 & \rho_\infty c_\infty & 0 \\ 0 & \rho_\infty c_\infty & 0 & 1 \\ 0 & -\rho_\infty c_\infty & 0 & 1 \end{bmatrix} \begin{Bmatrix} \rho' \\ u' \\ v' \\ p' \end{Bmatrix} \tag{20a}$$

and

$$\begin{Bmatrix} \rho' \\ u' \\ v' \\ p' \end{Bmatrix} = \begin{bmatrix} -\frac{1}{c_\infty^2} & 0 & \frac{1}{2c_\infty^2} & \frac{1}{2c_\infty^2} \\ 0 & 0 & \frac{1}{2\rho_\infty c_\infty} & -\frac{1}{2\rho_\infty c_\infty} \\ 0 & \frac{1}{\rho_\infty c_\infty} & 0 & 0 \\ 0 & 0 & \frac{1}{2} & \frac{1}{2} \end{bmatrix} \begin{Bmatrix} c_1 \\ c_2 \\ c_3 \\ c_4 \end{Bmatrix} \tag{20b}$$

Implementation of this boundary condition requires a knowledge of the underlying exit flow variables, ρ_∞, u_∞, v_∞, and p_∞. The first three quantities are time lagged whereas the exit pressure, p_∞, is kept constant.

5.3. Inlet Boundary

Here again two types of boundary conditions were used. The first was the reflective boundary condition procedure wherein three quantities have to be specified. The three chosen are the Riemann invariant

$$R_1 = u + \frac{2c}{\gamma - 1} = u_{-\infty} + \frac{2c_{-\infty}}{\gamma - 1}, \tag{21a}$$

the total pressure

$$p_{\text{total}} = p_{-\infty}\left(1 + \frac{\gamma - 1}{2} M^2_{-\infty}\right)^{\gamma/\gamma - 1}, \tag{21b}$$

and the inlet flow angle, which in this case is equivalent to

$$v_{\text{inlet}} = 0. \tag{21c}$$

The fourth quantity needed to update the points on this boundary is also a Riemann invariant but is extrapolated from the interior and is given by

$$\frac{\partial R_2}{\partial x} = 0, \tag{21d}$$

where

$$R_2 = u - \frac{2c}{\gamma - 1}.$$

In the above equations the quantities u and v are the velocities in the x and y directions, p is the pressure and c is the local speed of sound. Specifying the total pressure at the inlet results in the boundary condition being reflective.

A non-reflective or radiative one-dimensional boundary condition (Bayliss & Turkel 1982) was also implemented. As in the case of the exit boundary, it is assumed that at the upstream boundary the flow is linear, that is, the unsteadiness can be considered a linear perturbation to a steady flow. Using an analysis that is very similar to that used in developing the radiating boundary condition for the exit boundary we obtain the following condition at the inlet:

$$p'_t = \rho_{-\infty}(u_{-\infty} - c_{-\infty})(u'_t + u_{-\infty}u'_x). \tag{22}$$

At the upstream boundary, the Riemann invariant, R_1, and the flow angle, $v_{\text{inlet}} = 0$, are

still used. However, p_{total} is replaced by the condition that at the inlet, the flow is isentropic, which gives

$$p/\rho^{\gamma} = \text{constant} = p_{-\infty}/\rho_{-\infty}^{\gamma}, \tag{23}$$

and equation (21d) is replaced by equation (22).

The radiating boundary condition described above is basically one-dimensional in nature. Two-dimensional inlet boundary conditions (Giles 1988b) were also implemented. The inlet boundary conditions in terms of the one-dimensional characteristic variables are

$$\frac{\partial}{\partial t}\begin{Bmatrix} c_1 \\ c_2 \\ c_3 \end{Bmatrix} + \begin{bmatrix} v & 0 & 0 & 0 \\ 0 & v & \frac{1}{2}(c+u) & \frac{1}{2}(c-u) \\ 0 & \frac{1}{2}(c-u) & v & 0 \end{bmatrix}_{-\infty} \frac{\partial}{\partial y}\begin{Bmatrix} c_1 \\ c_2 \\ c_3 \\ c_4 \end{Bmatrix} = 0, \tag{24a}$$

$$\frac{\partial c_4}{\partial x} = 0. \tag{24b}$$

The transformation between the one-dimensional characteristic variables and the perturbation flow quantities are given by equation (20), with the quantities $(\ )_{\infty}$ replaced by the quantities $(\ )_{-\infty}$.

5.4. Upper and Lower Boundaries

The computations reported in this study assume that the flow is spatially periodic in the y-direction. The spatial interval of periodicity depends upon the airfoil count. (For example, in the 3-stator/4-rotor case, periodicity is imposed after every three stator airfoils and four rotor airfoils.) Further details regarding this boundary condition can be found in Rai (1987).

6. RESULTS

In this section, results obtained for the single-rotor/single-stator and four-rotor/three-stator configurations are presented. In particular, a comparison between the long-grid and short-grid computation with reflective boundary conditions and non-reflective boundary conditions will be made. In addition, the spectrum of the turbine tones and the variation of the amplitudes of the different modes in the far field will be presented for different cases.

The dependent variables are non-dimensionalized with respect to the far upstream pressure ($p_{-\infty}$) and density ($\rho_{-\infty}$). The free-stream velocities are

$$u_{-\infty} = M_{-\infty}\sqrt{\gamma}, \qquad v_{-\infty} = 0,$$

where $M_{-\infty} = 0{\cdot}07$ is the inlet Mach number. The pressure ratio across the turbine ($p_{\text{static}_{\text{exit}}}/p_{\text{total}_{\text{inlet}}}$) is 0·963. The rotor velocity was obtained so as to match the experimental flow coefficient (ratio of average inlet velocity to rotor speed) of 0·78 as given in Dring *et al.* (1982). The Reynolds number is 100,000/in. The kinematic viscosity was calculated using Sutherland's law and the turbulent eddy viscosity was calculated using the Baldwin–Lomax model. The calculations were performed at a

constant time-step value of about 0·16 (this translates into 500 time steps for the rotor to move through a distance equal to the distance between two successive blades).

6.1. Airfoil Surface Pressure Amplitudes

The first comparison is made between the long and the short grid computations for the single-rotor/single-stator case. Reflective boundary conditions are used in both computations. Figure 2 shows the pressure amplitudes on the stator for the two cases. The symbols in this figure are the experimental data of Dring *et al.* (1982). The pressure amplitude ($\tilde{C}_p$) is defined as

$$\tilde{C}_p = \frac{p_{\max} - p_{\min}}{\frac{1}{2}\rho_{\text{inlet}}\omega^2}$$

where ω is the rotor velocity and $p_{\max}$ and $p_{\min}$ are the maximum and minimum pressures that occur over a cycle. A cycle corresponds to the rotor moving by a distance equal to the distance between adjacent rotor or stator airfoils. The pressure amplitudes obtained in the short-grid computation show most of the qualitative features that are found in the experimental results. However, the numerical data show a wider large-amplitude region than that found experimentally. In addition, the predicted peak is to the left of the experimental peak, and the pressure amplitude minimum on the suction side seen in the experimental results ($x \approx -2{\cdot}4$) is absent in the computed results. The long grid computation yields an amplitude distribution closer to the experimental data. The position of the peak and the extent of the large amplitude region agree well with the data.

The improvement obtained using the long grid is due to the large grid spacing in the far field region of the outer grid, which attenuates propagating modes. However, one penalty incurred in using this approach is the excessive computer time needed to obtain a periodic state. A typical short grid computation for a 3-stator/4-rotor case to converge to a time periodic state (including convergence in the tonal acoustics) is about 20 cpu hours on a single processor of a CRAY YMP supercomputer. For a corresponding long grid computation, approximately five times as much computing time is required. Additionally, the time for convergence varies linearly with the number of airfoils, provided the extent of the upstream and downstream regions of the grid is the same. It should be mentioned that the time for convergence for flow quantities such

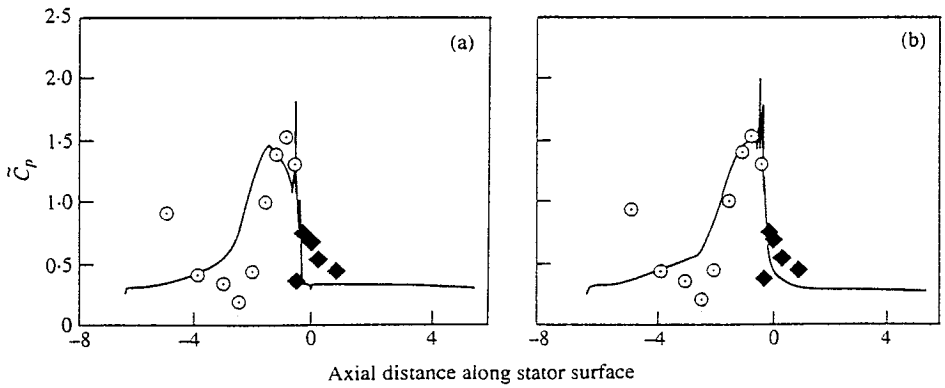

Figure 2. Pressure amplitude on stator surface for (a) short grid, (b) long grid for a 1-stator/1-rotor case: ○, suction surface; ◆, pressure surface.

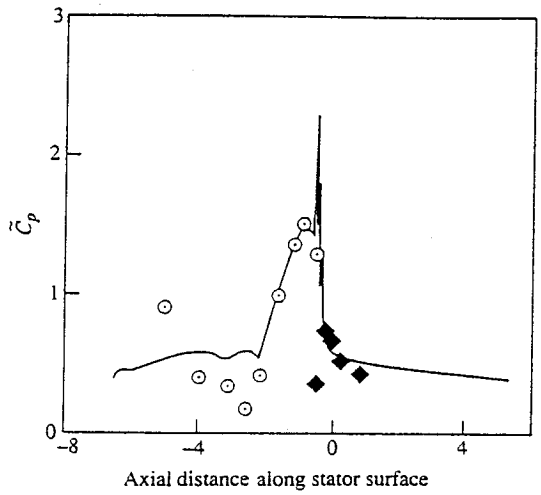

Figure 3. Pressure amplitude on stator surface for a 1-stator/1-rotor case (using nonreflective boundar conditions): ○, suction surface; ◆, pressure surface.

as pressure amplitudes on the airfoil surfaces and near field acoustics was considerabl less.

Figure 3 shows the computed surface pressure amplitude distribution obtained usin the short grid in conjunction with the one-dimensional non-reflective inlet and exi boundary conditions [see equations (18, 22)]. The agreement with the experimenta data is slightly better than that obtained on the long grid with reflective boundar conditions. It was found that the level of repeatability (solution periodicity in time with these boundary conditions was much better and the solution converged to a tim periodic state faster. In addition, turbine operating conditions were maintained unlik in Rai (1990), where the use of non-reflective boundary conditions required an iterativ process in which the Riemann invariant, R_2, (specified at the exit) had to be variec until the proper average exit pressure was obtained. The flow coefficient and th turbine pressure ratio differed from that obtained using the reflective boundar condition by less than 1%. (This will be shown later in Table 3.) Figure 4 shows th

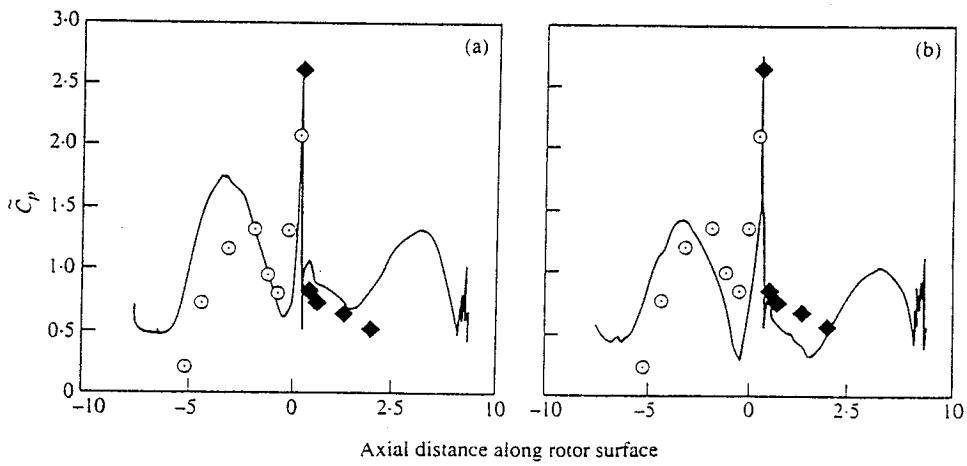

Figure 4. Pressure amplitude on rotor surface with a (a) reflective boundary conditions and (b) non-reflective boundary conditions for a 1-stator/1-rotor case: ○, suction surface; ◆, pressure surface.

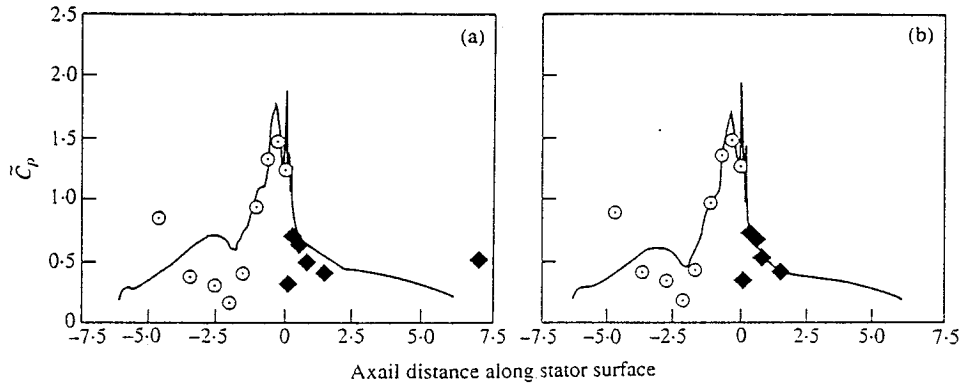

Figure 5. Pressure amplitude on stator surface for 3-stator/4-rotor case with (a) a short grid and (b) a long grid: ○, suction surface; ◆, pressure surface.

pressure amplitudes on the rotor for a short grid with and without reflective boundary conditions. It is seen that the amplitudes obtained using the non-reflective boundary conditions are generally lower.

In contrast to the single-stator/single-rotor case, the pressure amplitudes for the 3-stator/4-rotor case did not differ much for the long or short grid or for the reflective or non-reflective boundary conditions. For the single-stator/single-rotor case, an acoustic analysis (Tyler & Sofrin 1970) shows that every harmonic could have propagating modes whereas the 3-stator/4-rotor case does not have any propagating modes for the first two blade passing harmonics. The first two harmonics do have decaying modes. In the original experimental configuration, there are 22 stator airfoils and 28 rotor airfoils. For this case also, the acoustic analysis does not predict any propagating modes for the first two blade passing harmonics. Since the higher harmonics are usually much smaller in magnitude, the unsteady pressures that reach the computational boundaries in the 3-stator/4-rotor case are much smaller than that for the single-stator/single-rotor case. Hence, it is expected that the reflective properties of the boundary conditions would play a smaller role in determining the unsteady pressures on the airfoils for the 3-stator/4-rotor case. Figure 5 shows the pressure amplitudes on the stator surface for the short and long grids with reflective boundary conditions. Figure 6 shows the pressure amplitude for the short grid with

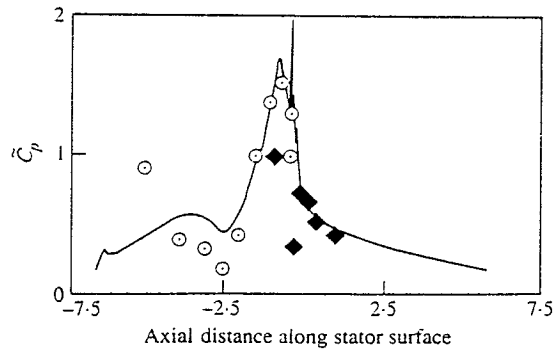

Figure 6. Pressure amplitude on stator surface for 3-stator/4-rotor case (using non-reflective boundary conditions): ○, suction surface; ◆, pressure surface.

non-reflective boundary conditions. Clearly there is an improvement over the resul depicted in Figure 2(a) and a slight improvement over that depicted in Figures 2(b) ar 3. The extent of the large amplitude region and the location of the pressure pea matches the experimental data. The slight improvement is due to a closer similarity the geometry with that of the experimental geometry. However, it should not b concluded that reflective properties of the computational boundaries are unimporta for the 3-stator/4-rotor case; they can still significantly alter the tonal acoustics in th linear region of the flow. The pressure amplitudes on the rotor surface for th 3-stator/4-rotor case also did not depend on the type of grid or the boundar conditions. The amplitudes on the rotor surface were very similar to that reporte previously by Rai & Madavan (1990).

Besides the pressure amplitudes, phase information can also be obtained. The phas of the low pressure peak on the stator suction surface [see Rai and Madavan (1990) fo details] for the 3-stator/4-rotor case did not depend on the type of grid or the boundar conditions. The numerical results compared well with experimental data of Dring *et a* (1982) and were similar to that reported by Rai & Madavan (1990).

6.2. Far Field Linear Behavior

The spectrum of turbine tones obtained from the computations is presented in th section. Recall that the Fourier modes predicted by the kinematical analysis ar denoted by p_{mn} [equation (3)], where m and n are related as given by equation (5). Th values of a_{mn} can be obtained by performing a Fourier decomposition of the pressur variation upstream and downstream of the turbine. The upstream results wer calculated at two chord-lengths upstream of the leading edge of the stator airfoils ar the downstream results were calculated at two chord-lengths downstream of the trailin edge of the rotor airfoils. Figure 7(a, b) shows the contribution of the axially aligne planar waves ($m = 0$) for the single-stator/single-rotor case. The x-axis corresponds t

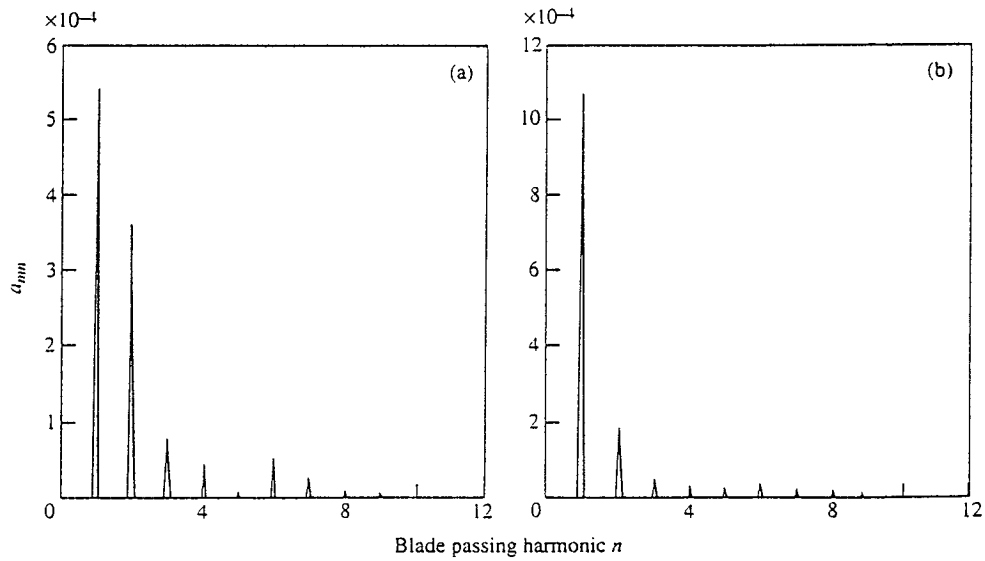

Figure 7. Spectrum of the $m = 0$ mode (a) upstream of the stator and (b) downstream of the rot (1-stator/1-rotor).

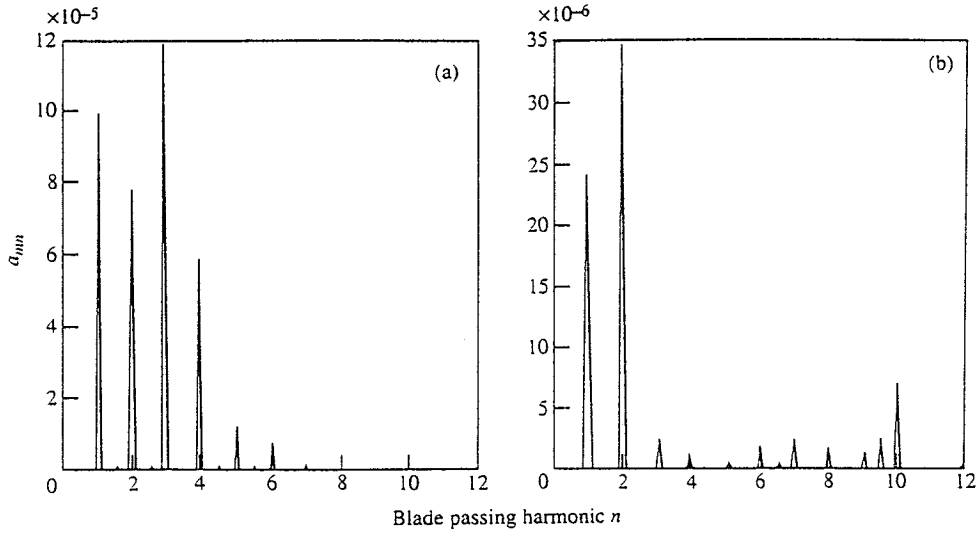

Figure 8. Spectrum of the (a) $m = 1$ and (b) $m = -1$ modes downstream of the rotor (1-stator/1-rotor).

harmonics of blade passing frequency and the y-axis corresponds to the computed coefficients, a_{mn}. It is seen that, in general, the amplitudes of the higher harmonics are smaller than the amplitudes of the lower harmonics. Equation (6) predicts that all these harmonics propagate without decay. The numerical results conform with this prediction [see Rangwalla & Rai (1990)]. Note that the contribution due to the subharmonics of blade passing frequency is very small (by two orders of magnitude) compared to the harmonics of that frequency, thus leading to the conclusion that, for this mode, the kinematical interactions dominate. It was also found that the contribution of the non-planar modes ($m \neq 0$) upstream of the stator was less by at least an order of magnitude when compared to the planar modes. Figure 8 shows the $m = 1$ and $m = -1$ modes downstream of the rotor. These modes are about an order of magnitude smaller than the planar mode. The subharmonic content is very small as in the $m = 0$ case.

The situation in the 3-stator/4-rotor case is different. For the planar case ($m = 0$), equation (5) predicts the existence of only the $n = 3, 6, 9, \ldots$ harmonics of blade passing frequency. Figure 9(a) shows the contribution of these planar waves upstream of the stator. Although the subharmonic content is more than in the single-stator/single-rotor case, most of the energy is seen to lie in the $n = 3$ and $n = 6$ harmonics. Figure 9(b) shows the contribution of the planar waves downstream of the rotor. It should be noted that the pressure variations downstream of the rotor are measured in the rotor frame of reference. Hence for the $m = 0$ modes, the kinematical analysis predicts the existence of only the $n = 4, 8, 12, \ldots$ harmonics of blade passing frequency. Once again, we notice a low level of subharmonic noise, thus leading to the conclusion that for this case the kinematical interactions dominate. It should be noted that, for the $m = 0$ modes, the subharmonic noise of the single-stator/single-rotor case is of the same order of magnitude as the 3-stator/4-rotor case than that in the single-stator/single-rotor case.

The $m = 1$ and $m = -1$ modes upstream of the stator are shown in Figure 10(a, b). Substituting $R = 4$ and $S = 3$ in equation (5), the positive integer values that are possible for n when $m = -1$ are $n = 1, 4, 7, \ldots$ and when $m = 1$, the positive integer values that n can take are $n = 2, 5, 8, \ldots$ We observe that the dominant frequencies

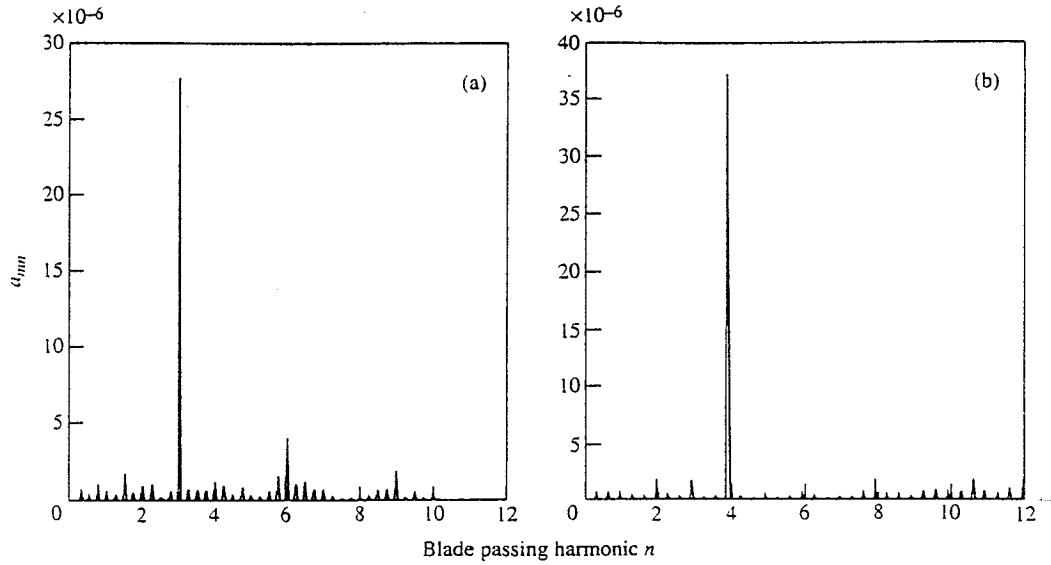

Figure 9. Spectrum of the (a) $m = 0$ mode upstream of the stator and (b) the $m = 0$ mode downstream o the rotor for the 3-stator/4-rotor case.

conform with the kinematical analysis. The same is true downstream of the rotor. Since the pressure variations downstream of the rotor are measured in the rotor frame o reference, R and S in equation (5) should be interchanged. Hence, for the $m = 1$ mode downstream of the rotor–stator pair, equation (5) predicts the existence o $n = 3, 7, 11, \ldots$ blade passing harmonics. Similarly, for the $m = -1$ mode, equation (5) predicts that the blade passing harmonics that can be present are given by $n = 1, 5, 9, \ldots$. The $m = 1$ and $m = -1$ modes downstream of the rotor are shown in Figure 10(c, d). Once again we observe that the dominant frequencies conform with the kinematical analysis.

The computations can also be used to study the propagation or decay of the various modes. To do this, either a long grid has to be used and the amplitudes of each mode calculated in the region of the grid where the solution has not suffered from numerical dissipation (due to grid coarseness) or a short grid with non-reflective boundary conditions should be used. A study of the numerical propagation or decay of the different modes has the advantage of determining the grid spacing required in the far field to maintain a propagating mode or to capture accurately the decay rate of a decaying mode. Additionally, the effect of boundary conditions on the different modes can be assessed.

Figure 11(a, b) shows the effect of grid coarsening on propagating waves for the 3-stator/4-rotor case. Figure 11(a) shows the amplitudes of three propagating modes [$a_{0,3}$, $a_{0,6}$ and $a_{0,9}$ as given by equation (8)] upstream of the rotor–stator pair. As propagating modes, these amplitudes should remain constant. However, the amplitudes do decay as the grid spacing in the axial direction increases; (the symbols indicate the axial location of the grid points). As expected, the higher harmonics decay faster because they have smaller wavelengths. In the present case, the wavelength of the (0, 3) mode is approximately 21·11 in. (536·2 mm), the wavelength of the (0, 6) mode is approximately 10·55 in. and the wavelength of the (0, 9) mode is about 7·04 in. From Figure 11(a) we see that numerical dissipation sets in when there are five or fewer mesh points within a wavelength. Figure 11(b) shows the amplitudes of the propagating

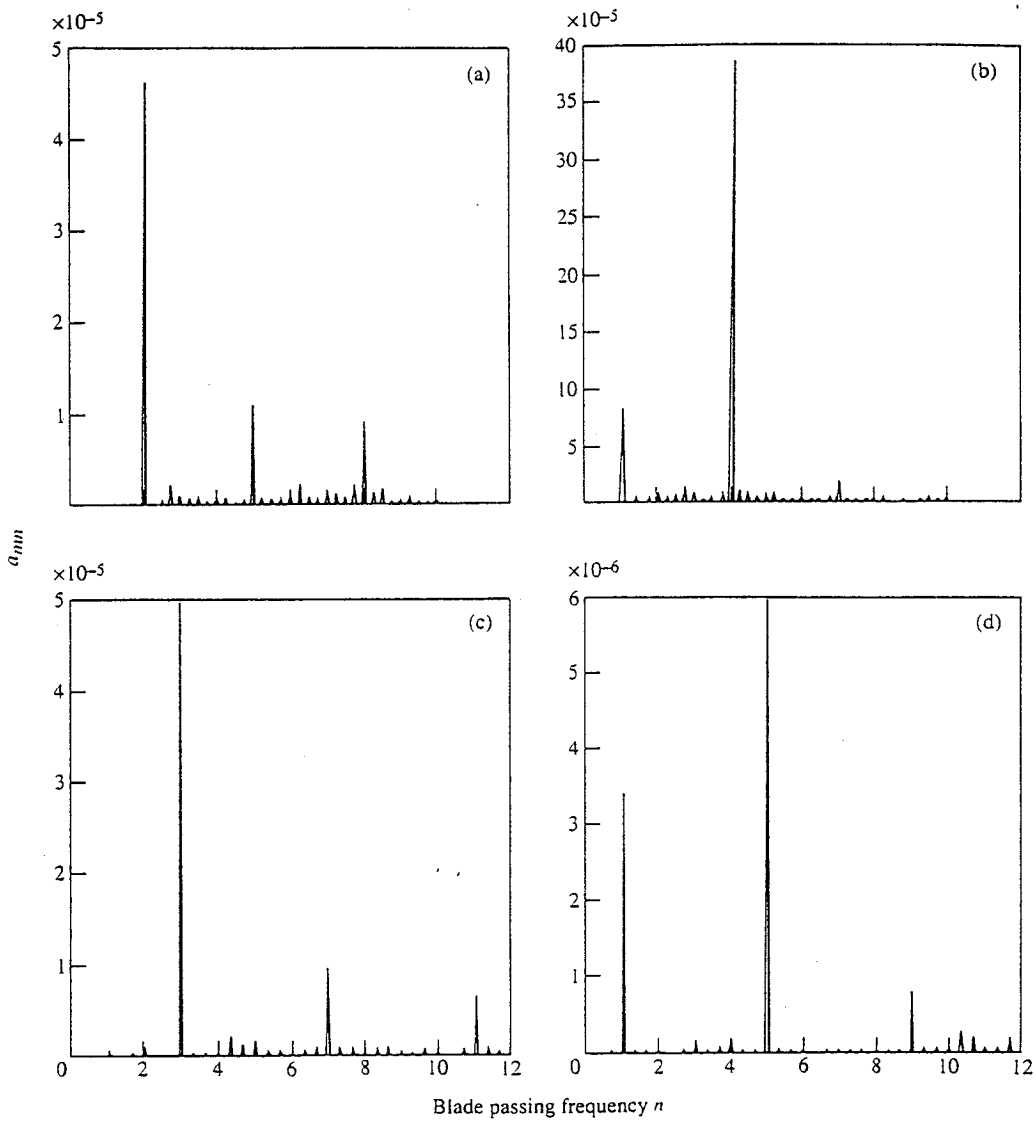

Figure 10. Spectrum of the (a) $m = 1$ and (b) $m = -1$ modes upstream of the stator and of the (c) $m = 1$ and (d) $m = -1$ modes downstream of the rotor (3-stator/4-rotor).

modes ($a_{0,4}$ and $a_{0,8}$) downstream of the rotor–stator pair. Unlike the upstream results, these amplitudes exhibit rapid variations near the rotor–stator pair. These oscillations eventually subside and the amplitudes remain constant till they monotonically decay because of grid coarsening. The rapid axial variation of the amplitudes immediately downstream of the rotor–stator pair is due to the nonuniformity of the mean flow. This nonuniformity is largely due to the velocity defects in the wakes of the rotor airfoils. The axial range over which the effect of this nonuniformity is felt depends upon the mode. It will be seen later that the rate of decay of the decaying modes and the axial wavelength of propagating modes can be significantly affected by the nonuniformity of the underlying mean flow. The effect of numerical dissipation due to grid coarseness downstream of the rotor–stator pair is similar to that observed in the upstream region. In the present case, the wavelengths of the $(0, 4)$ and $(0, 8)$ modes are approximately

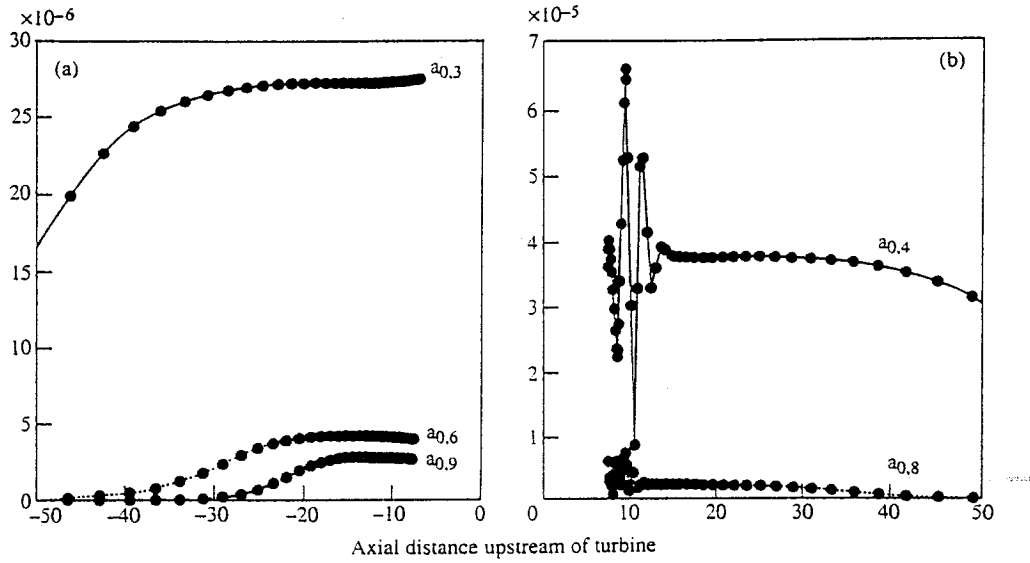

Figure 11. Axial variation of the amplitudes of some propagating modes (a) upstream of the stator and (b) downstream of the rotor (3-stator/4-rotor); ●, axial location of grid points.

20·96 and 10·48 in., respectively. In Figure 11(b) it is seen that numerical dissipation affects the propagating modes when the number of mesh points within a wavelength are five or less.

Figure 12(a, b) shows the instantaneous variation in the axial direction of the (0, 3) and (0, 4) modes. In the figure, the effect of grid coarsening on the waveform can be seen. Grid coarsening can affect the amplitude as well as the wavelength of the mode. The present numerical results seem to indicate that the wavelength variation due to grid coarseness is slight, as long as there are more than five grid points per wavelength.

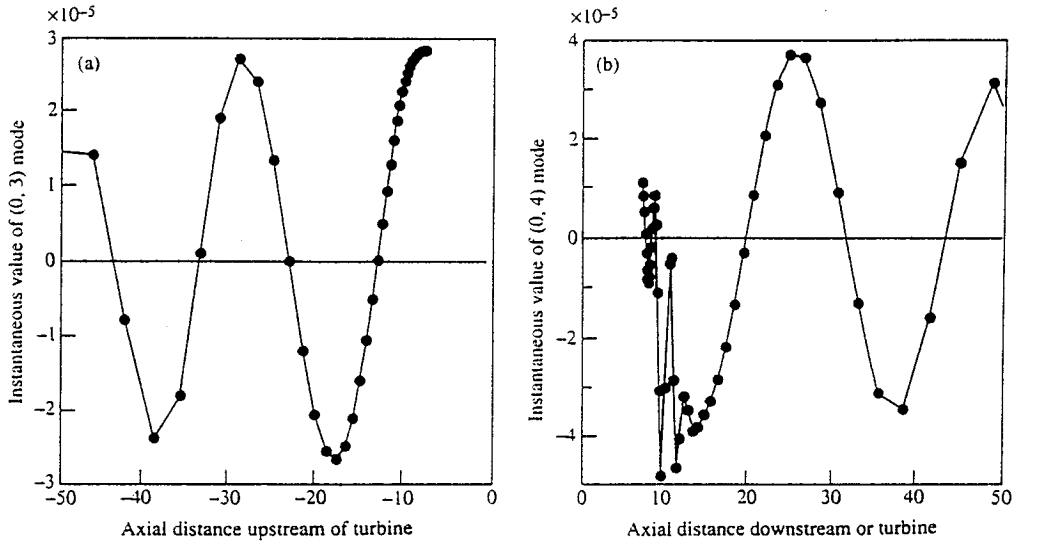

Figure 12. Instantaneous axial variation of the (a) (0, 3) mode upstream of the stator and (b) (0, 4) mode downstream of the rotor (3-stator/4-rotor); ●, axial location of grid points.

TABLE 1

Axial wavelengths of some propagating modes (upstream); 3-stator/4-rotor case. (Theory in parentheses)

	−2	−1	0	1	2
$n=1$		decaying			decaying
$n=2$	decaying			decaying	
$n=3$			20·54(21·11)		
$n=4$		20·81(21·63)			decaying
$n=5$	decaying			14·96(15·09)	
$n=6$			10·49(10·55)		
$n=7$		9·46(9·81)			14·15(14·48)
$n=8$	10·57(10·82)			8·11(8·41)	
$n=9$			7·03(7·04)		
$n=10$		6·35(6·58)			7·16(7·55)

However the amplitude can be significantly affected by grid coarseness and decays to about half its value when there are six grid points per wavelength.

Comparisons between the theoretical axial wavelengths and that obtained numerically are shown in the Tables 1 and 2 for the 3-stator/4-rotor case.

Table 1 shows comparisons upstream of the rotor–stator pair. In general, the results are good. The differences are less than the maximum grid spacing in the region where the wavelengths were measured. Table 2 shows a similar comparison downstream of the rotor–stator pair. The numerical results are generally in fair agreement with the theoretical predictions for all (m, n) modes where $m \leq 0$. The differences are of the same order as the maximum grid spacing in the region where the wavelengths were measured. However, the calculated wavelengths of the (m, n) modes where $m > 0$ do not agree well with theoretical predictions. It should be recalled that the theoretical prediction of axial wavelengths [equation (8)] was obtained under the assumption of a uniform mean flow. However, downstream of the rotor–stator pair, the underlying mean flow is not uniform due to the wakes of the airfoils. It is believed that this nonuniformity in the mean flow is the main reason for the discrepancy between the numerical results and theoretical predictions.

One objective of the present study is to see if non-reflective boundary conditions can be used along with a short grid to predict the tonal acoustics present in rotor–stator

TABLE 2.

Axial wavelengths of some propagating modes (downstream); 3-stator/4-rotor case. (Theory in parentheses)

	−2	−1	0	1	2
$n=1$		decaying			
$n=2$	decaying				decaying
$n=3$				decaying	
$n=4$			23·51(20·96)		
$n=5$		23·78(26·91)			
$n=6$	decaying				decaying
$n=7$				18·38(13·39)	
$n=8$			11·65(10·48)		
$n=9$		10·81(10·47)			
$n=10$	11·89(13·46)				20·81(11·12)

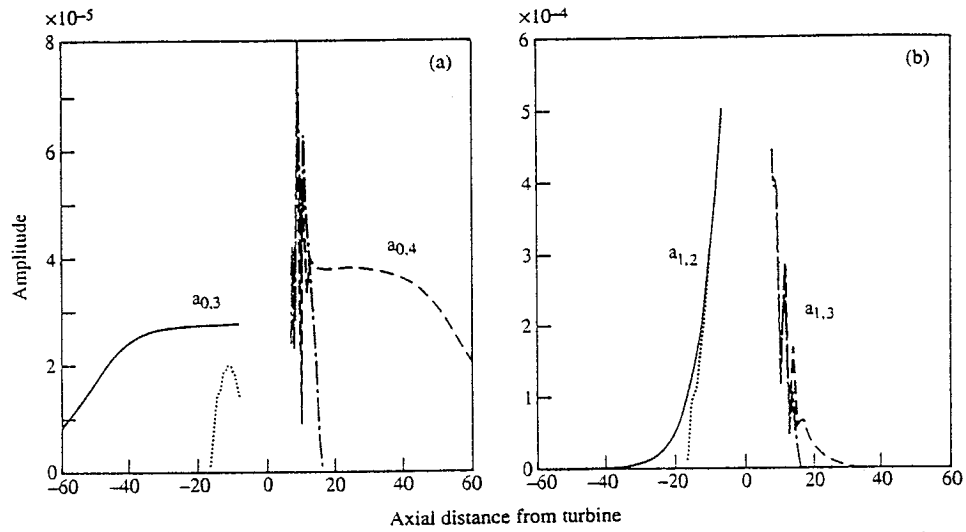

Figure 13. Comparison between a long grid solution and a short grid solution with reflective boundar conditions for (a) the (0, 3) mode upstream and (0, 4) mode downstream of the rotor–stator pair, and (b) th (1, 2) mode upstream and (1, 3) mode downstream of the rotor-stator pair. ——, - - -. Long grid; · · · · —·—·—, short grid.

interactions. Three different boundary conditions were compared. The first boundar condition was a reflective boundary condition as given in Rai & Madavan (1990). Thes boundary conditions have been widely used in the numerical simulations of rotor stator interactions. However, they are not adequate in the study of tonal acoustic because of their reflective properties. Figure 13(a, b) shows the comparison of sho and long grid calculations with reflective boundary conditions for the 3-stator/4-rotc case. In Figure 13(a) the axial variation of the amplitudes of two propagating mode are shown. The effect of using reflective boundary conditions can be seen in this figur At the exit boundary of the short grid, the amplitudes become zero whereas at the inl boundary, the amplitudes are very small.

The short and long grid solutions also do not compare well within the flow domai The short grid solutions do not show an axial region where the amplitudes remai constant. This is because a reflective boundary condition reflects any propagating moc back into the flow domain. As expected the long grid solution does exhibit an axi region over which the amplitudes remain constant. The reason for this is that th coarseness in the grids near the inlet and exit boundaries essentially dissipates th propagating waves, thus minimizing the effects of reflection. In contrast to th propagating modes, the effect of the reflective boundary conditions on the decayir modes is only significant near the boundaries. Figure 13(b) shows the axial variation the (1, 2) mode upstream of the stage and the (1, 3) mode downstream of the stag The results show that the amplitudes remain unaffected in the near field region of th airfoils. It should be recalled that these results are for the 3-stator/4-rotor case. For th case the boundary conditions did not significantly affect the pressure amplitudes on th airfoil surfaces. The amplitudes on the airfoil surfaces are mainly composed of th lower harmonics. For the 3-stator/4-rotor case, the lower harmonics decay wi increasing axial distance from the airfoils. Reflective boundary conditions do refle these modes but the effect of the reflection is confined to the region near th boundaries.

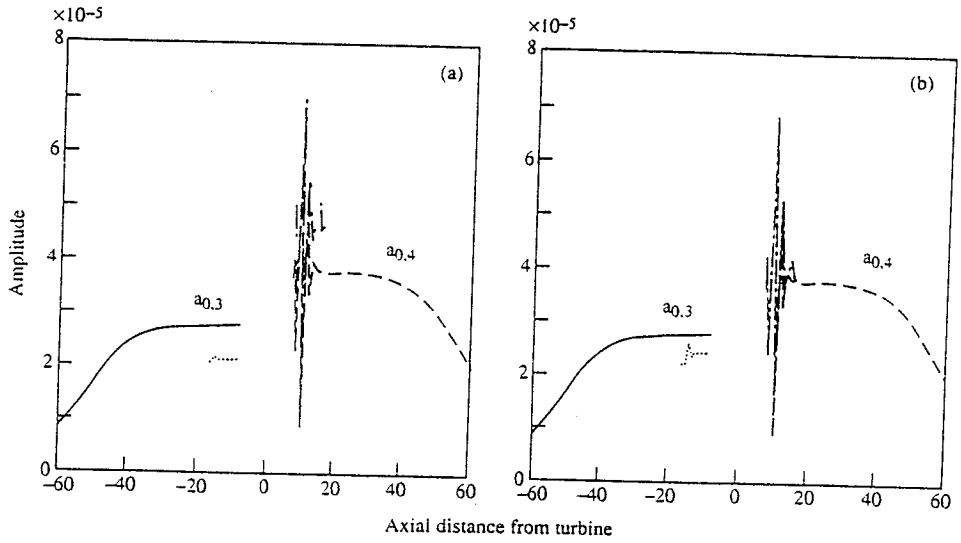

Figure 14. Comparison between a long grid solution and a short grid solution for the (0, 3) mode upstream and the (0, 4) mode downstream of the rotor–stator pair using the (a) one-dimensional non-reflective boundary condition and the (b) two-dimensional non-reflective boundary condition. ——, – – –, Long grid; · · · · ·, — — —, short grid.

Figures 14 and 15 show the axial variation of the amplitudes of the same modes [as in Figure 13(a, b)] obtained on the short and long grids with non-reflective boundary conditions. Figure 14(a, b) shows the upstream axial variation of the amplitudes of the (0, 3) mode and the downstream variation of the (0, 4) mode with one-dimensional boundary conditions [equations (18, 22)], and two-dimensional boundary conditions [equations (19, 24)], respectively. The variation of the amplitudes of the propagating

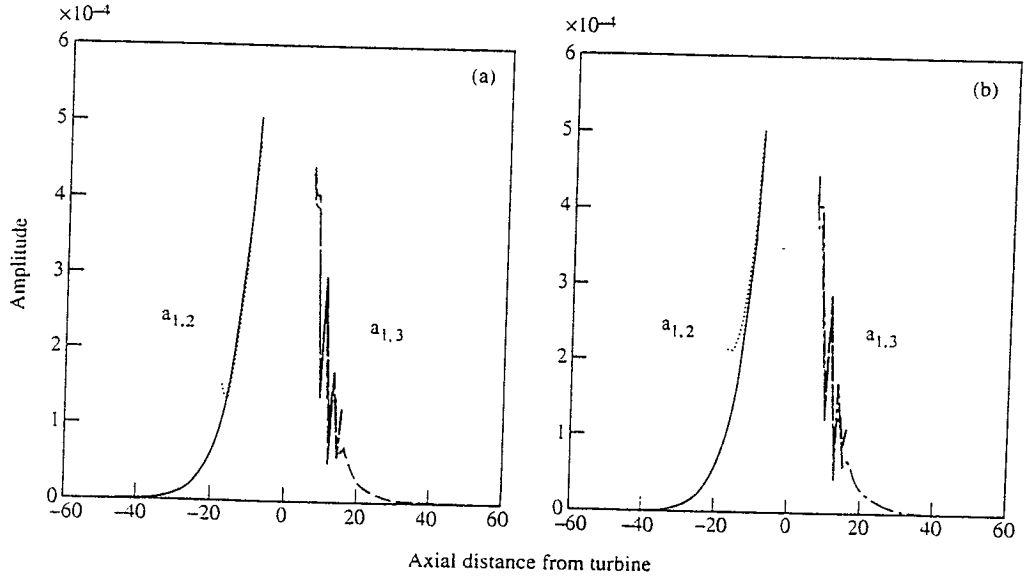

Figure 15. Comparison between a long grid solution and a short grid solution for the (1, 2) mode upstream and the (1, 3) mode downstream using (a) the one-dimensional non-reflective boundary condition and (b) the two-dimensional non-reflective boundary condition. ——, – – –, Long grid; · · · · ·, — — —, short grid.

TABLE 3.
Converged operating conditions

	Experimental	Reflective B.C.	1-D B.C.	2-D B.C.
$\frac{p_{static_{exit}}}{p_{total_{inlet}}}$	0·963	0·963	0·9636	0·963
$Velocity_{inlet}$	0·083	0·084	0·083	0·084
$p_{total_{inlet}}$	1·0034	1·0034	1·0031	1·0034

modes for the short grid case are similar to that for the long grid. However, the overall levels are a bit different. This difference may be due to the difference in the converged operating conditions as shown in Table 3. The differences between the short and long grid solutions with one-dimensional boundary conditions are larger than that obtained with the two-dimensional boundary conditions. The results also show some reflectivity at the boundaries, as evidenced by the oscillations in the amplitudes near the upstream boundaries. Figure 15(a, b) shows the upstream axial variation of the (1, 2) mode and the downstream axial variation of the (1, 3) mode. In contrast to the propagating modes, the amplitudes of these modes remain unaffected in the near-field region of the airfoils. At the inlet and exit computational boundaries of the short grid, there are differences between the results obtained between the long and short grid solutions. However, the solutions obtained by the one-dimensional and two-dimensional non-reflective boundary conditions are slight. Examination of other decaying modes show the same overall behavior, i.e., the amplitudes of the modes remain nearly unaffected in the near-field regions of the airfoils.

The amplitudes of the decaying modes vary exponentially in the upstream and downstream directions [equation (11)]. The rate of decay depends upon the underlying mean flow and the temporal and spatial frequencies of the mode as given in equation (12). [It should be recalled that equation (12) is derived under the assumption of linear perturbations to a steady uniform mean flow]. The axial and transverse Mach numbers of the underlying mean flow upstream and downstream of the turbine is obtained from the numerical solutions. The mean flow quantities in nondimensional units are given in Table 4. The nondimensional velocity of the rotor airfoils (V_R) is 0·1051282. The quantities M_x, M_y and M_R in equation (9) can be evaluated from U_x, U_y, V_R and the sonic velocity of the underlying mean flow.

Figure 16(a, b) shows the axial variation of the amplitudes of some decaying modes upstream and downstream of the rotor–stator pair. It should be noted that equations (11) and (12) yield only the rate of decay and not the amplitude level. Hence in Figure 16(a, b), only the slopes of the curves are of interest. The behavior of these modes upstream of the rotor–stator pair is in excellent agreement with the linear theory in the region where the grid is sufficiently fine. In the far upstream region, the numerical

TABLE 4.
Mean flow quantities

	Upstream	Downstream
Axial velocity, U_x	0·0842535	0·0864004
Transverse velocity, U_y	0·00	0·0701666
Sonic velocity, c	1·1829303	1·1774635

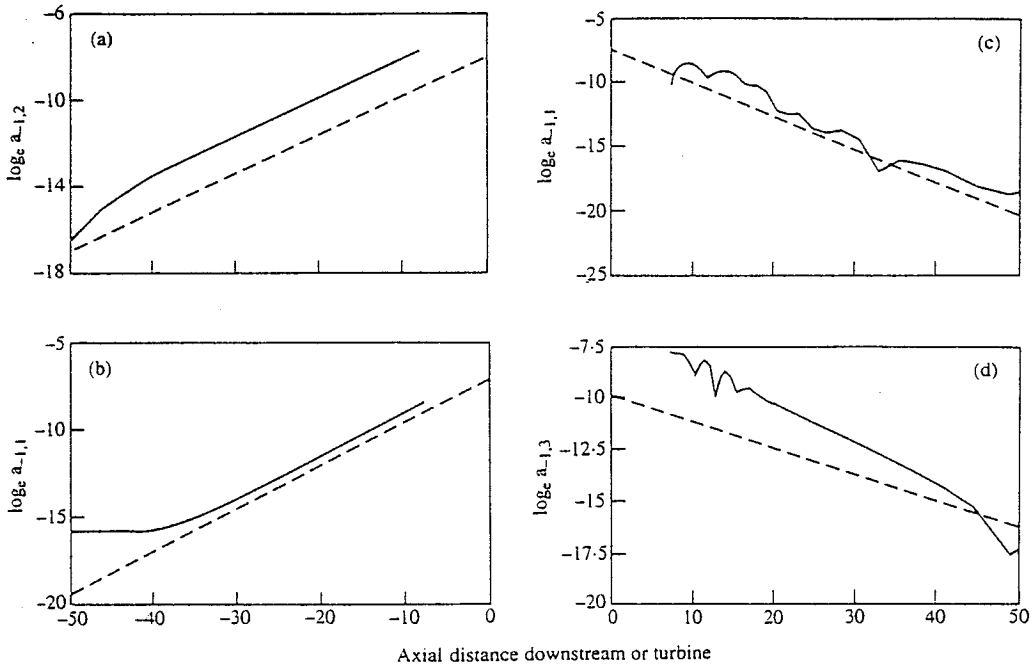

Figure 16. Comparison between numerical and theoretical decay rates upstream for (a) mode (1, 2) and (b) mode (−1, 1) upstream of the stator and for (c) mode (−1, 1) and (d) mode (1, 3) downstream of the rotor: ——, numerical; - - -, theoretical.

solution deviates from the theoretical exponential decay because of the very coarse grid in this region.

Downstream of the rotor–stator pair, a difference between the numerical results and the linear theory is seen [Figure 16(c, d)]. The axial variation of the natural logarithm of amplitude of the (−1, 1) mode ($\log a_{-1,1}$) is shown in Figure 16(c). Even though the overall decay matches that of the theoretical exponential decay, the numerical variation of the amplitude is not a "pure" exponential. Rather, the axial variation of the computed amplitude is exponential as well as oscillatory in nature. This behavior was observed for all (l, k) modes, where $l < 0$. Figure 16(d) shows the axial variation of the natural logarithm of the amplitude of the (1, 3) mode. The decay of this mode is exponential, however, the decay rate does not match the theoretical prediction. This difference between the numerical and theoretical decay rates was observed for all (l, k) modes where $l > 0$. It should be recalled that one of the assumptions underlying the theoretical results is a uniform mean flow. However, downstream of the rotor–stator pair, the underlying mean flow does deviate from a uniform flow because of the wakes of the rotor airfoils. This deviation is much more than the deviation upstream of the rotor–stator pair due to potential effects. It is believed that the nonuniformity in the mean flow is the main reason for the discrepancy between the numerical results and theory.

7. SUMMARY

This study focuses on the numerical computation of tones in rotor–stator interactions. the numerical predictions are obtained by solving the thin-layer Navier–Stokes equations on a system of patched grids. The mode-cotent of interaction tone noise is

obtained for two different airfoil counts and is shown to conform with a kinematica analysis of the flow. In addition, the propagation characteristics of different modes are compared with the predictions of linear theory. Numerically computed pressure amplitudes on the surface of the airfoils are compared with experimental data.

The effects of both reflective and non-reflective boundary conditions on the calculated flow field were assessed. It was found that for the short-grid calculations non-reflective boundary conditions had to be used in order to predict the tona acoustics in the flow field. Use of non-reflective boundary conditions becomes more important for those cases where there is a high energy content in the propagating modes. (The single-stator/single-rotor case for example, had propagating lower harmonics. These harmonics had high energy content. Reflection of these harmonics from the computational boundaries resulted in a degradation of the computed pressure amplitudes on the airfoil surfaces.) It was also shown that reflective boundary conditions can be made to behave essentially as non-reflective boundary conditions with the use of appropriately long grids in the upstream and downstream regions. The long grid approach in conjunction with an increasing grid cell size in the far upstream and downstream regions results in numerical dissipation of propagating modes, thus avoiding the problems due to reflections at the computational boundaries.

ACKNOWLEDGEMENT

This study was partially supported by NASA Marshall Space Flight Center. Some o the computing resources were provided by the NASA OAST NAS programme. The authors would like to thank Dr R. P. Dring of United Technologies Research Cente for providing the turbine airfoil geometries used in this investigation.

REFERENCES

BAYLISS, A. & TURKEL, E. 1980 Radiation boundary conditions for wave-like equations *Communications on Pure and Applied Mathematics* **33,** 707–725.

BAYLISS, A. & TURKEL, E. 1982a Far field boundary conditions for compressible flows. *Journa of Computational Physics* **48,** 182–199.

BAYLISS, A. & TURKEL, E. 1982b Outflow boundary conditions for fluid dynamics. *SIAM Journal on Scientific and Stastical Computing* **3,** 250–259.

DORNEY, D. J., DAVIS, R. L., EDWARDS, D. E. & MADAVAN, N. K. 1990 Unsteady analysis o hot streak migration in a turbine stage. AIAA Paper No. 90–2354.

DORNEY, D. J. 1992 Numerical simulations of unsteady flows in turbomachines. PhD. Thesis The Pennsylvania State University, Department of Aerospace Engineering, University Park Pennsylvania, U.S.A.

DRING, R. P., JOSLYN, H. D., HARDIN, L. W. & WAGNER, J. H. 1982 Turbine rotor–stato interaction. *ASME Journal of Engineering for Power* **104,** 729–742.

ERDOS, J. I., ALZNER, E. & MCNALLY, W. 1977 Numerical solution of periodic transonic flo through a fan stage. *AIAA Journal* **15,** 1559–1568.

GIBELING, H. J., WEINBERG, B. C., SHAMROTH, S. J. & MCDONALD, H. 1986 Flow through compressor stage. Report R86-910004-F, Scientific Research Associates, Glastonbury, CT U.S.A.

GILES, M. B. 1988a Stator/rotor interaction in transonic turbine. AIAA Paper No. 88-3093.

GILES, M. B. 1988b Non-reflecting boundary conditions for the euler equations. Repo CFDL-TR-88-1, MIT Computational Fluid Dynamics Laboratory.

GOLDSTEIN, M. E. 1974 Aeroacoustics. NASA Report SP-346.

GUNDY-BURLET, K. L., RAI, M. M., STAUTER, R. C. & DRING, R. P. 1991 Temporarily an spatially resolved flow in a two stage axial compressor: Part 2-Computational assessmen *ASME Journal of Turbomachinery* **113,** 227–232.

GRIFFIN, L. & MCCONNAUGHEY, H. 1989 Prediction of the aerodynamic environment and heat transfer for rotor/stator configurations. ASME Paper No. 89-GT-89.

JORGENSON, P. C. E. & CHIMA, R. V. 1988 An explicit Runge-Kutta method for unsteady rotor/stator interaction. AIAA Paper No. 88-0049.

JORGENSON, P. C. E. & CHIMA, R. V. 1989 An unconditionally stable Runge Kutta method for unsteady flows. AIAA Paper No. 89-0205.

KOYA, M. & KOTAKE, S. 1985 Numerical analysis of fully three-dimensional periodic flows through a turbine stage. *ASME Journal of Engineering for Gas Turbines and Power* **107**, 945–952.

LEWIS, J. P., DELANEY, R. A. & HALL, E. J. 1987 Numerical prediction of turbine vane-blade interaction. AIAA Paper No. 87-2149.

MADAVAN, N. K., RAI, M. M. & GAVALI, S. 1989 Grid refinement studies of turbine rotor–stator interaction. AIAA Paper No. 89-0325.

RAI, M. M. 1986 An implicit conservative zonal boundary scheme for euler equation calculations. *Computers and Fluids* **14**, 99–131.

RAI, M. M. 1987 Navier–Stokes simulations of rotor–stator interaction using patched and overlaid grids. *AIAA Journal of Propulsion and Power* **3**, 387–396.

RAI, M. M. 1989 Three-dimensional Navier–Stokes simulations of turbine rotor–stator interaction; Parts 1 & 2. *AIAA Journal of Propulsion and Power* **5**, 305–319.

RAI, M. M. & MADAVAN, N. K. 1990 Multi-airfoil Navier–Stokes simulations of turbine rotor-stator interaction. *ASME Journal of Turbomachinery* **112**, 377–384.

RANGWALLA, A. A., MADAVAN, N. K. & JOHNSON, P. D. 1991 Application of an unsteady Navier–Stokes solver to transonic turbine design. *AIAA Journal of Propulsion and Power* **8**, 1079–1086.

RANGWALLA, A. A. & RAI, M. M. 1990 A kinematical/numerical analysis of rotor–stator interaction noise. AIAA Paper No. 90-0281.

RAO, K. V., DELANEY, R. A. & DUNN, M. G. 1992a Vane-blade interaction in a transonic turbine. Part 1-Aerodynamics. AIAA Paper No. 92-3323.

RAO, K. V., DELANEY, R. A. & DUNN, M. G. 1992b Vane-blade interaction in a transonic turbine. Part 1-Heat transfer. AIAA Paper No. 92-3324.

TYLER, J. M. & SOFRIN, T. G. 1970 Axial flow compressor noise studies. *SAE Transactions* **70**, 309–332.

VERDON, J. M. 1989 The unsteady flow in the far field of an isolated blade row. *Journal of Fluids and Structures* **3**, 123–149.

AIAA-94-2835

Unsteady Navier-Stokes Computations for Advanced Transonic Turbine Design

Akil A. Rangwalla
MCAT Institute
NASA Ames Research Center
Moffett Field, CA 94035-1000

30th AIAA/ASME/SAE/ASEE Joint Propulsion Conference

June 27-29, 1994 / Indianapolis, IN

UNSTEADY NAVIER-STOKES COMPUTATIONS FOR ADVANCED TRANSONIC TURBINE DESIGN

Akil A. Rangwalla†
MCAT Institute, Mountain View, CA

Abstract

This paper deals with the application of a three-dimensional, time-accurate Navier-Stokes code for predicting the unsteady flow in an advanced transonic turbine. For such advanced designs, prior work in two dimensions has indicated that unsteady interactions can play a significant role in turbine performance. These interactions affect not only the stage efficiency but can substantially alter the time-averaged features of the flow. This work is a natural extension of the work done in two dimensions and addresses some of the issues raised therein. These computations are being performed as an integral part of an actual design process and demonstrate the value of unsteady rotor-stator interaction calculations in the design of turbomachines. Results in the form of time-averaged pressures and pressure amplitudes on the airfoil surfaces are shown. In addition, instantaneous contours of pressure and Mach number are presented in order to provide a greater understanding of the inviscid as well as the viscous aspects of the flowfield. Relevant secondary flow features such as cross-plane contours of total pressure and span-wise variation of mass-averaged quantities are also shown.

Introduction

The traditional design of new turbines has relied upon empirical correlations, extensive experimental data, and a technology data base comprising previous designs. This design process has proven very reliable for new designs that do not deviate very much from those in the existing data base. However, a more general predictive capability is needed when the operating conditions of a new design demand radical deviations from the data base.

Considerable progress has been made in using computational fluid dynamics (CFD) to predict flows within turbomachines. Much of the early work has focused on predicting the flow in airfoil cascades. An extensive body of experimental and numerical results in the literature deals with a wide variety of two-and three-dimensional cascade geometries. While such methods of analysis of flows in isolated airfoil rows have helped improve our understanding of flow phenomena in turbomachinery and have gained widespread acceptance in the industrial community as a design tool, they do not yield any information regarding the unsteady effects arising out of rotor-stator aerodynamic interaction. However, it is becoming increasingly important to consider interaction effects in the design of new generation turbines. This has come about due to the constraints of low weight, small size, high specific work per stage, high efficiency, and durability, which results in very high turning angles and unconventional airfoil shapes, potentially giving rise to nonlinear unsteady interactions.

In the past few years, advanced transonic turbines have been designed by Pratt and Whitney in support of the Consortium for CFD Application in Propulsion Technology sponsored by NASA Marshall Research Center. These turbines are characterized by very high flow turning angles (160° per stage) and relatively high loading coefficients. The current status of turbine design technology is shown in Fig. 1 (private communication, L. Griffin, NASA Marshall Space Flight Center). The figure shows the turning angles and turbine loading coefficients of some existing turbine designs. The figure shows two designs (the G^3T and the G^2OT) that have turning angles of 160° which is 20° higher than the traditional design limit of 140°.

Numerical methods that simulate the unsteady flow associated with rotor-stator configurations have been developed in recent years. References 1–3 present a zonal approach for solving the unsteady, thin-layer, Navier-Stokes equations for rotor-stator configurations in a time-accurate manner, both in two and three dimensions. The present work is an application of the three-dimensional rotor-stator code described in Ref. 3, to evaluate the design of the advanced Gas Generator Oxidizer turbine designed by Pratt and Whitney, and will henceforth be referred to as the G^2OT. It should be mentioned that the first application of an unsteady two-dimensional Navier-Stokes solver for design purposes was carried out for the G^3T (Ref. 4). The numerical predictions were obtained at a constant radius corresponding to the midspan of the rotor airfoils. The primary issue was the effect of unsteady interactions on boundary layer separation. The results from the unsteady two-dimensional analysis led to design modifications (Ref. 4) and provided the designers with a better understanding of the physics of the flow. The results also validated the concept of using high turning angles and high specific work per stage. One out-

† Research Scientist. Senior Member, AIAA

come was the possibility of using single-stage turbines for certain applications, thus considerably simplifying the design process. This directly influenced the design of the G^2OT. The unsteady two-dimensional code was again used to aid in the design of the G^2OT and was reported in Ref. 5. The flow was predicted at a constant radius which was equal to the midspan of the rotor airfoil. Results were obtained for two power settings (100% and 70%) and it was found that the turbine loads were within the tolerances specified by design requirements and were acceptable. The two-dimensional analysis used in Ref. 4-5 contained quasi-three-dimensional source terms to account for stream tube contraction effects (Ref. 6). The numerical algorithm was an extension of that previously reported in Ref. 7.

One drawback of the two-dimensional analysis is that it is not complete. Since the flow is three-dimensional, the issue of secondary flow influencing flow features such as strength and position of the shocks has to be addressed. Other issues such as the effect of unsteady interactions on the end-wall boundary layers have to be assessed. Hence a three-dimensional interaction study was initiated.

In this paper, the three-dimensional as well as some two-dimensional results for the G^2OT will be presented. The two-dimensional results were obtained for two power settings (100% and 70%) whereas the three-dimensional results were obtained for only the 100% power setting. Comparisions will be made wherever possible. In particular, it was found that there were similarities as well as differences between the two-dimensional and three-dimensional results. The overall loading on the airfoils obtained from the three-dimensional analysis at midspan compared fairly with the two-dimensional predictions. However, some of the details such as strength and positions of the shocks differed. This also resulted in weaker unsteady interaction predictions by the three-dimensional calculations.

Two grid systems (one with twice as many points in the radial direction than the other) were used for a limited grid independance study. Each grid system contains multiple patched and overlaid grids as described in Ref. 3. These grids can move relative to one another to allow for the relative motion of the rotor airfoils with respect to the stator airfoils.

Numerical Method

The numerical method solves the unsteady, three-dimensional, thin-layer Navier-Stokes equations. The Navier-Stokes equations in three dimensions are nondimensionalized and transformed to a curvilinear time-dependent coordinate system, and a thin-layer approximation is then made. The unsteady, thin-layer, Navier-Stokes equations are solved using an upwind-biased finite-difference algorithm. The method is third-order-accurate in space and second-order-accurate in time. Several iterations are performed at each time step, so that the fully implicit finite-difference equations are solved to ensure a time-accurate solution. Further details of the method can be found in Ref. 3.

Boundary Conditions

The boundary conditions required when using multiple zones can be broadly classified into two types. The first are the zonal conditions which are implemented at the interfaces of the computational meshes, and the second are the natural boundary conditions imposed on the surface and the outer boundaries of the computational mesh. The treatment of the zonal boundary conditions can be found in Ref. 2. The natural boundary conditions used in this study are discussed below.

Airfoil Surface Boundary

The boundary conditions on the airfoil surfaces are the "no-slip" condition and adiabatic wall conditions. It should be noted that in the case of the rotor airfoil, "no-slip" does not imply zero absolute velocity at the surface of the airfoil, but rather, zero relative velocity. In addition, the derivative of pressure in the direction normal to the wall surface is set to zero.

Exit Boundary

The flow in the axial direction is subsonic at the exit boundary and hence only one flow quantity has to be specified. The flow quantity chosen in this study is the exit static pressure as a function of radius. To completely specify the flow variables at the boundary, four other flow quantities are extrapolated from the interior. The four chosen are the Reimann invariant,

$$R_1 = u + \frac{2c}{\gamma - 1}$$

the entropy,

$$S = \frac{p}{\rho^\gamma}$$

and the velocities in the transverse directions. One disadvantage of this type of boundary condition is that the pressure waves that reach the boundary are reflected back into the flow domain. However, this boundary condition was chosen since, in general, it provides greater control on the turbine operating conditions and results in the correct pressure drop and mass flow

through the turbine.

Inlet Boundary

The flow at the inlet boundary is subsonic. Four quantities need to be specified at this boundary. The four chosen were the Reimann invariant,

$$R_1 = u + \frac{2c}{\gamma - 1}$$

the total pressure as a function of radius,

$$p_{total} = p_{inlet}\left(1 + \frac{\gamma - 1}{2} M^2_{inlet}\right)^{\frac{\gamma}{\gamma - 1}}$$

and the inlet flow angles,

$$\frac{v_{inlet}}{u_{inlet}} = tan(\theta)$$

and

$$\frac{w_{inlet}}{u_{inlet}} = tan(\phi)$$

The fifth quantity needed to update the points on this boundary is also a Reimann invariant that is extrapolated from the interior and is given by

$$R_2 = u - \frac{2c}{\gamma - 1}$$

In the above equations, the quantities u and v and w are the velocities in the axial (x) tangential (θ) and the radial (r) directions, p is the pressure and c is the local speed of sound. Specifying the total pressure at the inlet results in a reflective boundary condition, but together with the specification of the exit static pressure, has the advantage of determining uniquely the turbine operating conditions.

Periodic Boundaries

Turbomachines are designed with unequal airfoil counts in the stator and rotor rows in order to minimize vibration and noise. A complete viscous simulation including all of the airfoils in the stator and rotor rows is yet impractical in a design environment. The approach used here is to assume that the ratio of the number of stator to rotor airfoils is a ratio of two small integers. This is achieved by scaling the stator or the rotor geometries such that the blockage remains the same. Periodicity conditions are then imposed over the composite pitch. For the case of the G^2OT turbine, the number of stator airfoils is 20 and the number of rotor airfoils is 42. By changing the number of stator airfoils to 21 and rescaling the stator airfoils by a factor of 20/21, a stator to rotor airfoil count of 1 to 2 is achieved. The calculation assumes that the flow exhibits spatial periodicity over one stator airfoil and two rotor airfoils. Note that the pitch of one rescaled stator airfoil is equal to the composite pitch of two rotor airfoils.

Geometry and Grid System

A schematic diagram of the G^2OT is shown in Fig. 2. This is a single stage turbine that is designed to operate in the transonic regime. It is characterized by very high turning angles and high specific work.

Figures 3a-b show the system of overlaid grids used to discretize the flow domain. The figure shows the fine grid with 51 grid points in the spanwise direction. Figure 3a shows the grid at the midspan. Each airfoil has two zones associated with it; an inner zone and an outer zone. The inner zone contains an O-grid that is generated using an elliptic grid generator. This grid is clustered near the airfoil surface in order to resolve the viscous effects. The outer zone is discretized with an H-grid and is generated algebraically. The inner and outer grids overlap one another. This positioning of the inner and outer grids facilitates information transfer between the two zones. The outer H-grids of the stator airfoils and rotor airfoils overlap and slip past each other as the rotor airfoils move relative to the stator airfoils. Figure 3b shows the surface grid (minus the casing). Here, the grid in the tip clearance region can also be seen. This grid was also generated by means of an elliptic grid generator and maintains metric continuity with the inner O-grid. The fine grid contains approximately 940000 grid points whereas the coarse grid has half as many.

Results

It should be mentioned that the numerical method has been validated both in two and three-dimensional applications. In particular, the ability to predict the time-averaged pressures and pressure amplitudes on airfoil surfaces and total pressure losses in airfoil wakes have already been demonstrated for turbines as well as for compressors (see Refs. 1-4, 7, 8).

G^2OT Two-Dimensional Computations

A brief description of the two-dimensional results (Ref. 5) will first be presented for the purpose of comparison with the three-dimensional results. Two-dimensional predictions were obtained for two power settings. The first setting is at 100% power and the second is at 70% power. The operating conditions for

the two power settings are shown in Table I.

	100% Power	70% Power
Inlet Mach No.	0.46	0.54
Inlet Reynolds No.	$2.6 \times 10^6/inch$	$1.1 \times 10^6/inch$
RPM	7880	6232
Inlet P_{total}	$542.77psia$	$313.82psia$
Exit P_{static}	$200.00psia$	$144.5psia$
Inlet T_{total}	$1307.02°R$	$1080.88°R$

Table I. Turbine operating conditions

Static Pressure Variation on Airfoils Figures 4 and 5 show the time-averaged and unsteady envelope of static pressure on the airfoil surfaces for the two different power settings, respectively. The pressure coefficient on the surface of the stator airfoils in this case is defined as

$$C_p = \frac{p_{static}}{p_{total_{inlet}}}$$

where p_{static} is either the time-averaged static pressure on the surface of the airfoil (to obtain the time-averaged pressure distribution) or the maximum or minimum pressure over a cycle (which results in the pressure envelope). The time averaging is performed over a cycle which corresponds to the rotor airfoils moving through two airfoil pitches. The pressure coefficient on the surface of the rotor airfoils is defined as

$$C_p = \frac{p_{static}}{p_{total(relative)_{rotorinlet}}}$$

Here, the pressure is normalized with respect to the time-averaged relative inlet total pressure to the rotor rows. The figures show that the results of the two power settings are qualitatively similar. The predicted pressure amplitudes are slightly smaller for the 70% power setting than for the design setting (100% power). The pressure distribution indicates a weak (nearly stationary) shock on the suction surface of the stator airfoil that impinges on the rotor suction surface near the leading edge (Ref. 5). It is this shock that accounts for the moderately high pressure amplitudes near the leading edge of the rotor airfoils. The pressure distributions also indicate a shock near the trailing edge of the rotor airfoils. This second shock is nearly stationary with respect to the moving rotor airfoils. It should be noted that these are two-dimensional results at constant radius. In the three-dimensional case, the interaction effects are found to be less severe due to the relaxation effects of the spanwise direction.

G^2OT Three-dimensional results

The results for the three-dimensional computations of the G^2OT for the 100% power setting are presented in this section. These results were obtained by integrating the governing equations and boundary conditions described earlier. A modified version of the Baldwin-Lomax turbulence model (Refs. 9-11) was used to determine the eddy viscosity. The modification involves the use of a blending function that varies the eddy viscosity distribution smoothly between the blade and endwall surfaces. Further details can be found in Refs. 10-11. The kinematic viscosity was calculated using Sutherland's law.

Static Pressure Variation on Airfoils Figures 6-8 show the time-averaged and unsteady envelope of static pressure on the stator and rotor airfoils at three spanwise locations. Figures 6a-8a show the pressure variations on the stator airfoil at the hub, the midspan and at the casing, whereas Figs. 6b-8b show the variations at the hub, the midspan and at the tip of the rotor airfoils. These results were obtained by the fine grid calculations and do not show any significant differences when compared with those obtained from the coarser grid. The level of unsteadiness on the stator airfoils is small compared to that on the rotor airfoils. The amplitudes also are smaller at the casing than at the hub. The figures seem to indicate the existence of a weak shock (made clearer by contour plots) on the suction surface of the stator near the hub. The pressure amplitudes on the rotor airfoil are larger. The rotor airfoils are unloaded considerably at the tip. However, it was found that this is very localized near the tip region and is not very critical. The predicted pressure amplitudes of the three-dimensional results at midspan, are smaller than the two-dimensional results. This is mainly due to the difference in the strength of the predicted axial gap shock.

Figures 9a-b show the comparisions of the time-averaged pressures between the three-dimensional and the two-dimensional results. On the stator airfoil, the two-dimensional calculations predict a lower unloading at the airfoil nose than that shown by the three-dimensional calculations. It should be noted that the two-dimensional calculations were performed on a surface of constant radius. Quasi-three-dimensional source terms associated with stream-tube contraction were included in the calculation, but the terms associated with radius variation were not. To properly account for these terms, the two-dimensional calculations would have to be performed on a cylindrical surface with an axially varying radius. The overall loading on the rotor airfoils compares better. However, the details are different. In particular, the position and strength of

the trailing edge shock on the suction surface is different. Also, other details that were present in the two-dimensional calculations, such as a large local variation on the suction surface, is absent in the three-dimensional results.

Instantaneous Mach Number Contours Figures 10a-c show instantaneous Mach number contours at 20%, 50% (midspan), and 80% of span respectively. These results were obtained for the fine grid system. At 20% of span, the shock near the trailing edge of the rotor airfoil can be seen. At this location, an axial gap shock was also seen. However, unlike the two-dimensional calculations the three-dimensional calculations predict an intermittent axial gap shock. At midspan (Fig. 10b), the shock in the axial gap region is much weaker, whereas there is no shock at the downstream location. In fact, it was found that the radial extent of the axial gap shock varied with time with a maximum extent of about 50%. Figure 10c shows the Mach contours at 80%. The contours seem to indicate that there might be unsteady separation on the suction surface of the rotor airfoils. Recall that the turning angles in this turbine are very high, and there is a concern about massive boundary layer separation under the influence of unsteady interactions. The numerical calculations do not predict massive boundary layer separation, as indicated by the Mach number contours, thus increasing the confidence in the design.

Instantaneous Static Pressure Contours Figures 11a-c show the instantaneous pressure contours at 20% 50% (midspan) and 80% of span respectively. These contours basically highlight the inviscid features of the flow. As expected, the rotor shock near the hub can be seen.

Mass-Averaged Quantities versus Span Figure 12 shows the mass-averaged meridonial angle versus normalized span at four different axial stations. The axial stations correspond to the inlet of the turbine, the midgap, half a chord downstream of the rotor airfoil, and about one and a half chord lengths downstream of the rotor airfoil. The figure does show that, to a large extent, the flow turns about 160° through the stage, however, it also shows a region of underturning at the midspan. Figure 13 shows the mass-averaged radial pitch angle. Recall from the schematic of the G^2OT (Fig. 2) that the casing angle is $-30°$ at the inlet, and is positive aft of the rotor (approximately 11.75°). This is reflected in the mass averaged pitch. Figures 14-17 show the variation of the mass-averaged Mach number, the relative Mach number (relative with respect to the rotating rotor airfoils), the absolute total pressure and the relative rotational total pressure. One surprising aspect of the results is the local increase in total pressure losses at the midspan.

Time-Averaged Contours Figures 18a-b show the time-averaged contours of the relative rotational total pressure at midgap and half a chord length downstream of the rotor airfoils. The circumferential extent of Fig. 18a equals the circumferential pitch between two successive stator airfoils whereas that of Fig. 18b equals the pitch between two rotor airfoils. Also, it should be noted that the time averaging is done in two different frames of reference. At the midgap (Fig. 18a) the frame of reference is stationary, whereas, downstream of the rotor airfoils (Fig. 18b) it is rotating. The contours at the midgap do show the expected (nearly uniform in span) stator wake along with the hub and casing secondary flows. However, aft of the rotor blades, at the midspan, a region of slightly higher losses exists. This was also observed in the mass-averaged numerical data (Figs. 16-17). Figures 19a-b show the time-averaged contours of Mach number relative to the rotor airfoils at the same axial location. The relative Mach number of the flow is subsonic at the midgap, but downstream of the rotor it becomes supersonic and eventually shocks.

Summary

A detailed numerical calculation of the three-dimensional unsteady flow in an advanced gas generator turbine is presented. The computational results are obtained by solving the three-dimensional, thin-layer, Navier-Stokes equations on a system of overlaid grids. The numerical results do capture many aspects of the flow that could aid in the understanding of the flow. In addition, the results do not indicate any significant boundary layer separation, (an object of concern). The unsteady loadings were found to be within acceptable limits.

The present results indicate that a proper understanding of the unsteady interaction effects could play an important role in the design of advanced gas generator turbines.

ACKNOWLEDGEMENT

This study was partially supported by NASA Marshall Space Flight Center. Computing resources were partially provided by the NAS program.

REFERENCES

1. Rai, M. M., "Navier - Stokes Simulations of Rotor-Stator Interaction Using Patched and Overlaid Grids," AIAA Journal of Propulsion and Power, Vol. 3, No. 5, pp. 387-396, Sep. 1987.

2. Rai, M. M., "Three-Dimensional Navier-Stokes Simulations of Turbine Rotor-Stator Interaction; Part 1 & 2," AIAA Journal of Propulsion and Power, Vol. 5, No. 3, pp. 305-319, May-June 1989.

3. Madavan, N. K., Rai, M. M. and Gavali, S., "A Multi-Passage Three-Dimensional Navier - Stokes Simulation of Turbine Rotor-Stator Interaction," Journal of Propulsion and Power, Vol. 9, pp. 389-396, May-June 1993.

4. Rangwalla, A. A., Madavan, N. K. and Johnson, P. D., "Application of an Unsteady Navier-Stokes solver to Transonic Turbine Design," AIAA Journal of Propulsion and Power, Vol. 8, No. 5, pp. 1079-1086, September-October 1992.

5. Rangwalla, A. A., "Unsteady Flow Calculation in a Single Stage of an Advanced Gas Generator Turbine." Invited paper at the Fifth Conference on Advanced Earth-to-Orbit Propulsion Technology, at NASA Marshall Space Flight Center, Huntsville, Alabama, May 19-21, 1992.

6. Chima, R. V., "Explicit Multigrid Algorithm for Quasi-Three-Dimensional Viscous Flows in Turbomachinery," Journal of Propulsion and Power, Vol. 3, No. 5, Sept-Oct. 1987, pp. 397-405.

7. Rai, M. M., and Madavan, N. K., "Multi-Airfoil Navier-Stokes Simulations of Turbine Rotor-Stator Interaction ," Journal of Turbomachinery, Vol. 112, pp. 377-384, July 1990.

8. Gundy-Burlet, K. L., Rai, M. M., Stauter, R. C., and Dring, R. P., "Temporarily and Spatially Resolved Flow in a Two Stage Axial Compressor: Part 2-Computational Assessment," ASME Journal of Turbomachinery, vol 113, pp. 227-232, April 1991.

9. Baldwin, B. S., and Lomax, H., "Thin Layer Approximation and Algebraic Model for Separated Turbulent Flow," AIAA Paper No. 78-257, 1978.

10. Dorney, D. J., and Davis, R. L., "Navier-Stokes Analysis of Turbine Blade Heat Transfer and Performance," Journal of Turbomachinery, Vol. 114, pp. 795-806, 1992.

11. Vatsa, V. N., and Wedan, B. W., "Navier-Stokes Solutions for Transonic Flow over a Wing Mounted in a Wind Tunnel," AIAA Paper No. 88-0102.

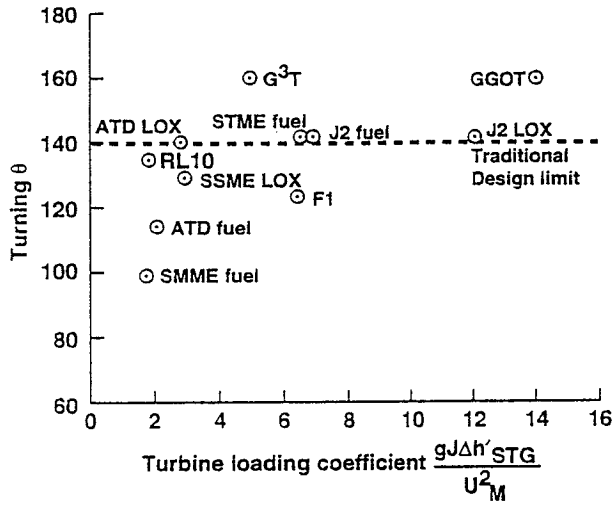

Fig. 1 Current status of turbine design technology.

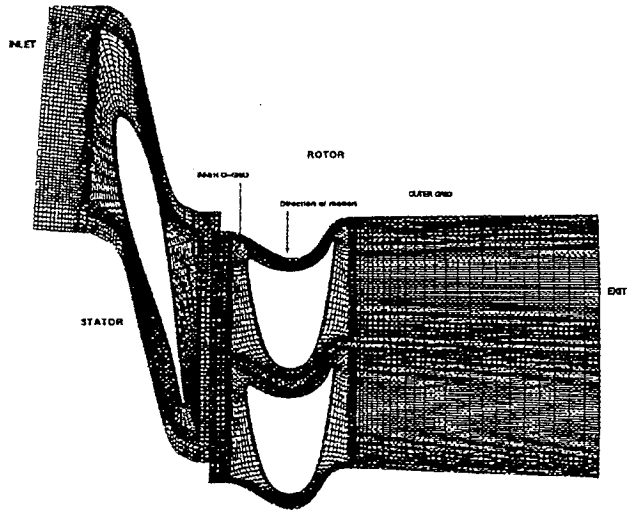

Fig. 3a Rotor-stator airfoil grid systems for the G^2OT, at mid-span

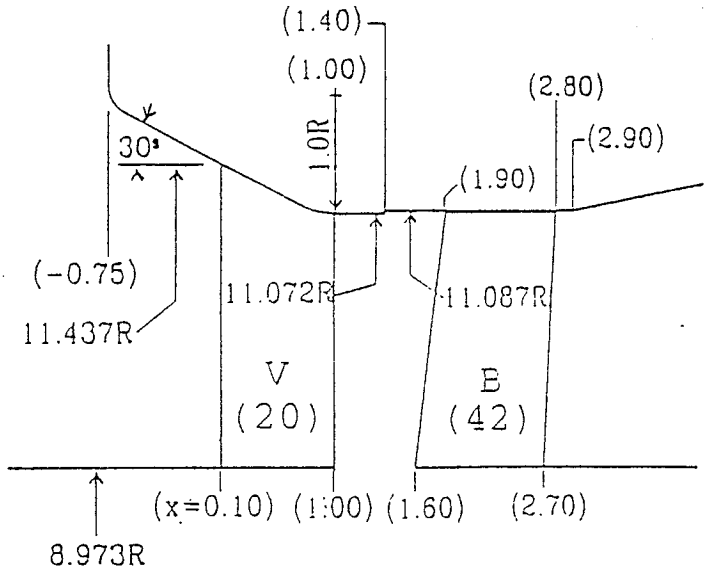

Fig. 2 Schematic of G^2OT flow path.

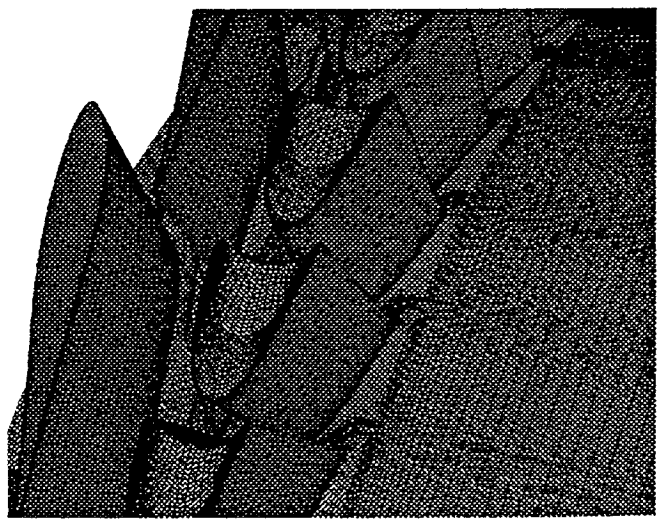

Fig. 3b Rotor-stator airfoil grid systems for the G^2OT, surface grid.

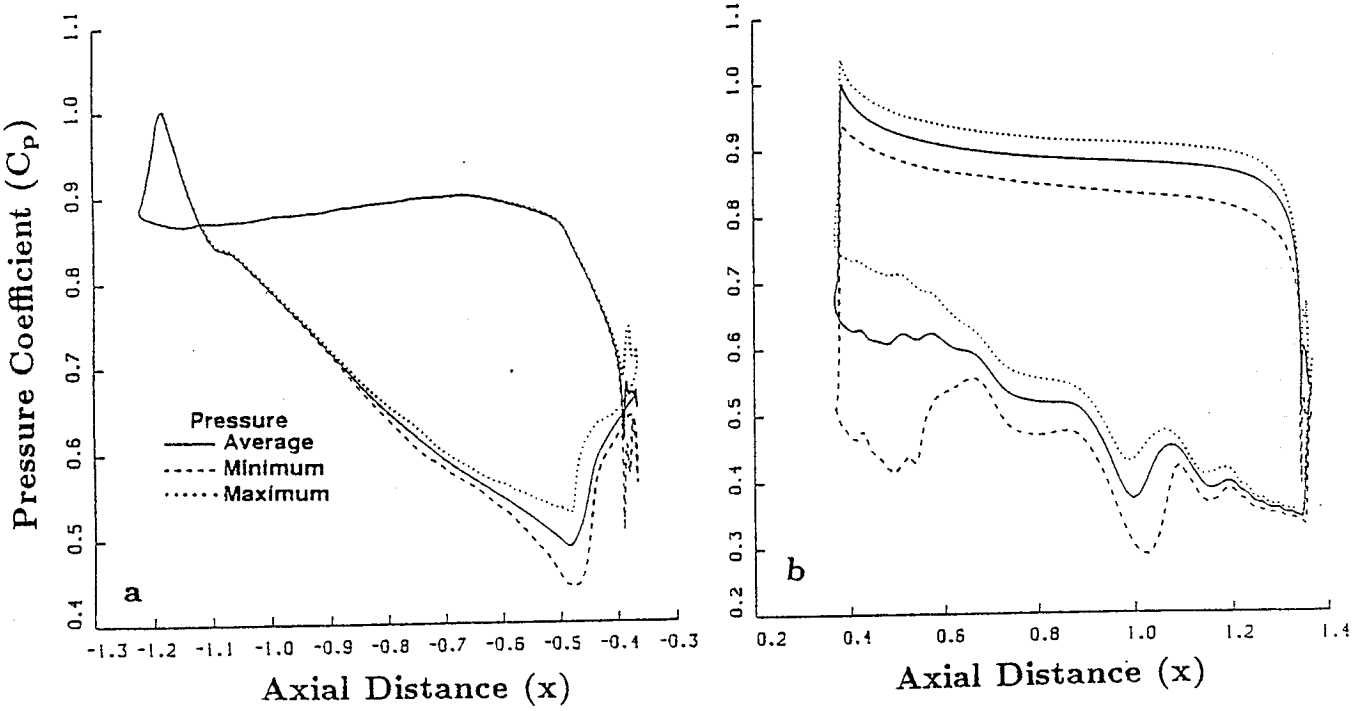

Fig. 4 Static pressure variation on (a) stator and (b) rotor airfoil surfaces for the G^2OT (100% power).

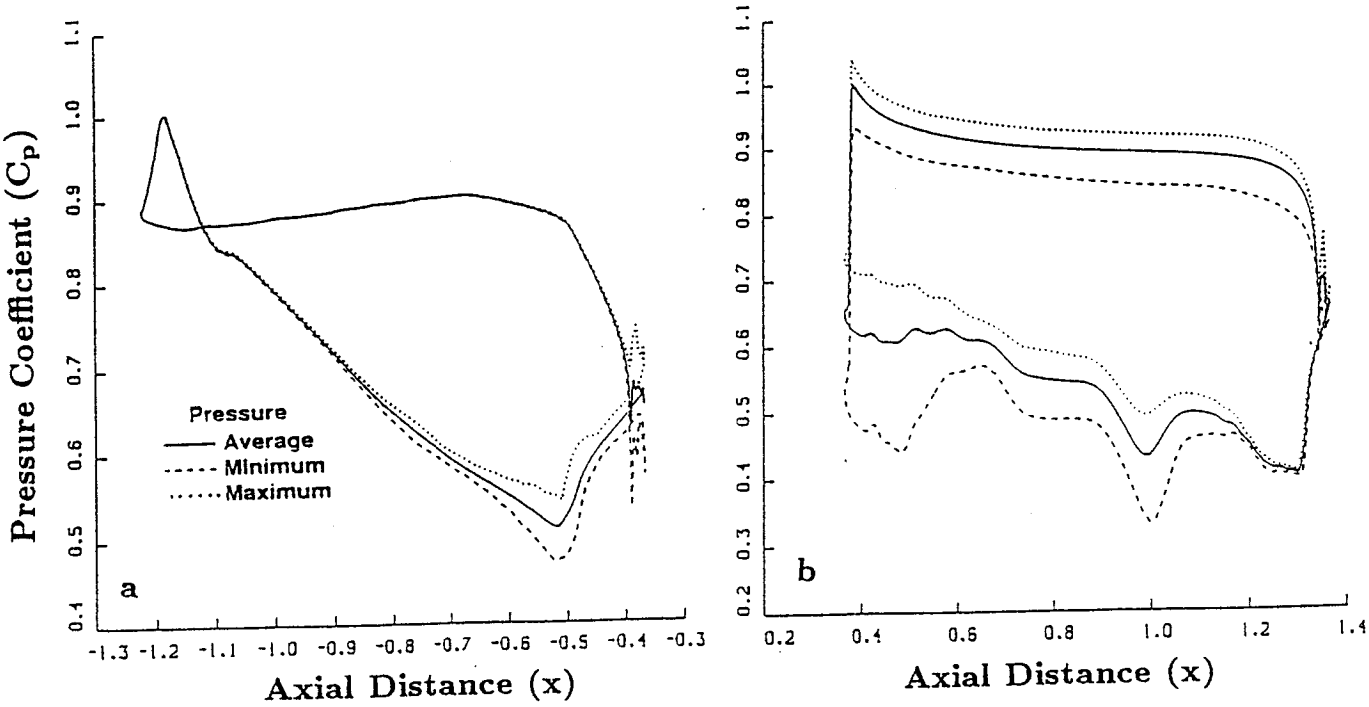

Fig. 5 Static pressure variation on (a) stator and (b) rotor airfoil surfaces for the G^2OT (70% power).

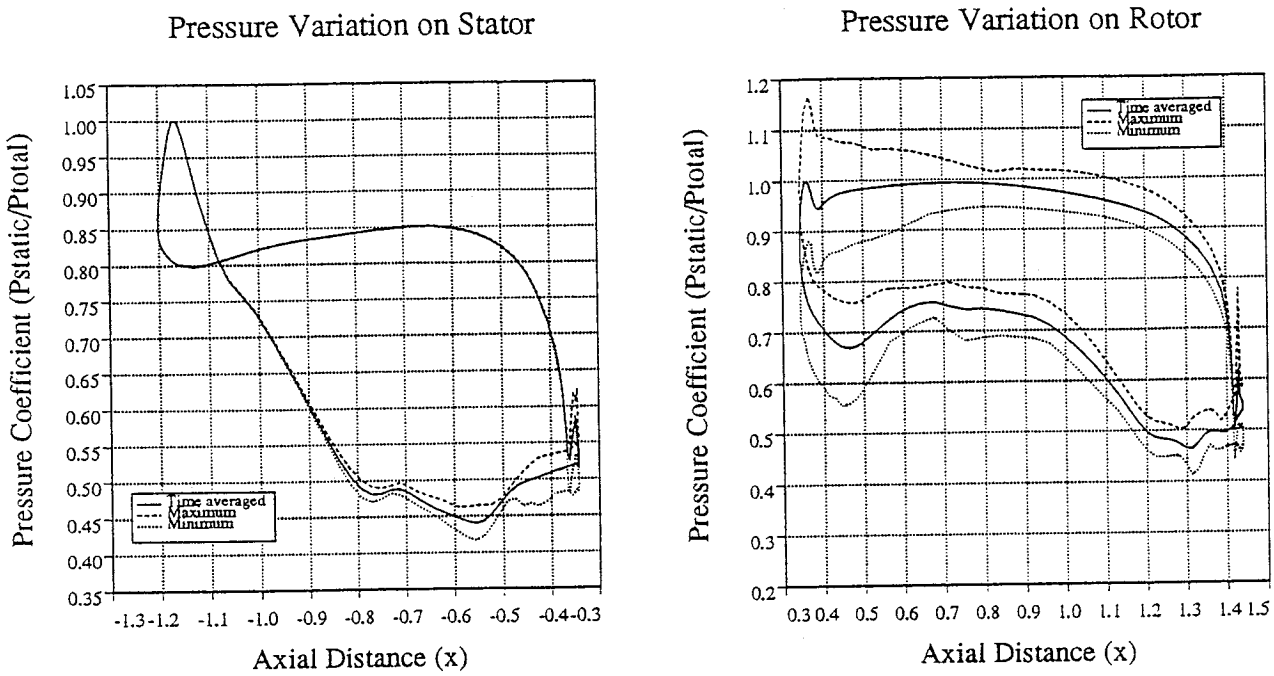

Fig. 6 Static pressure variation on (a) stator and (b) rotor airfoil surfaces for the G^2OT (Hub).

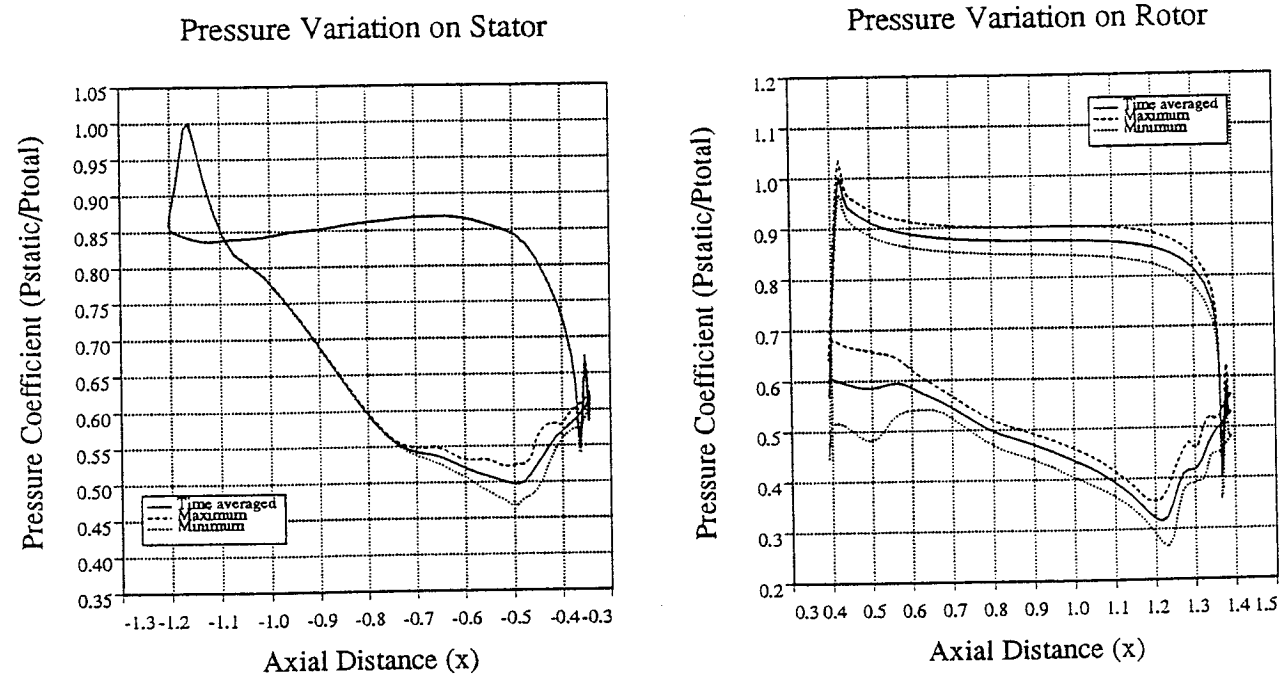

Fig. 7 Static pressure variation on (a) stator and (b) rotor airfoil surfaces for the G^2OT (Mid-span).

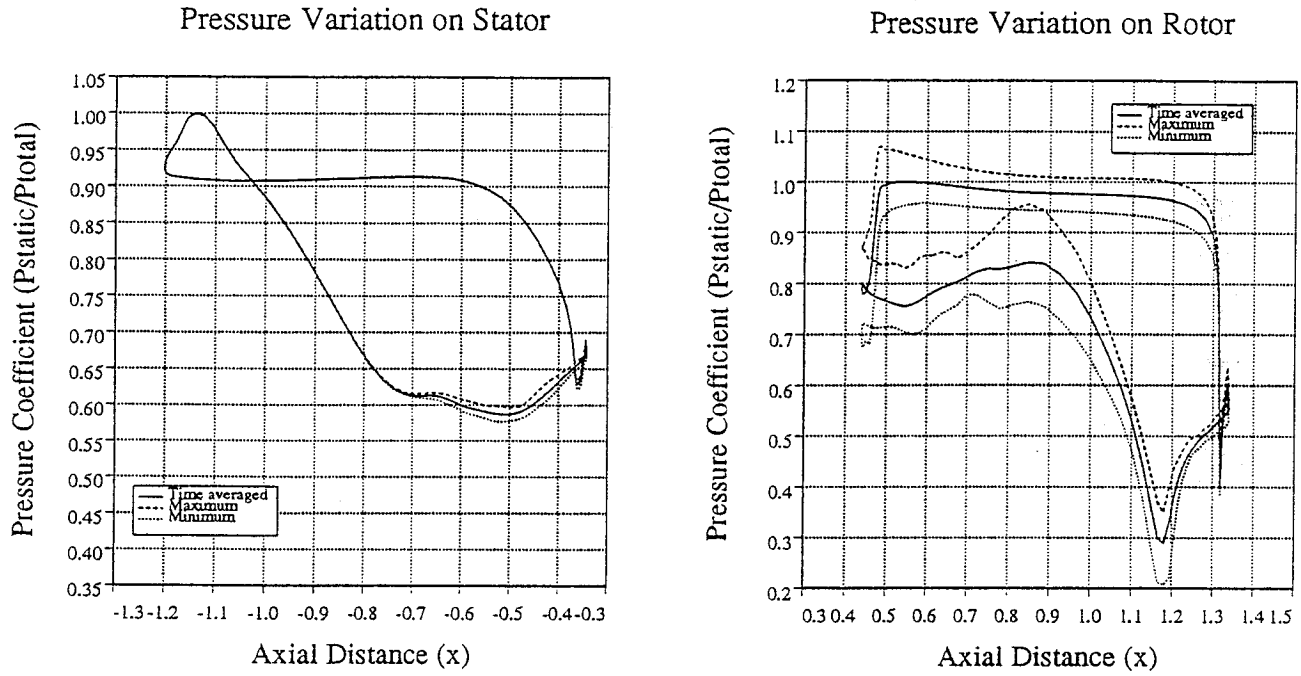

Fig. 8 Static pressure variation on (a) stator (casing) and (b) rotor airfoil (tip) for the G^2OT.

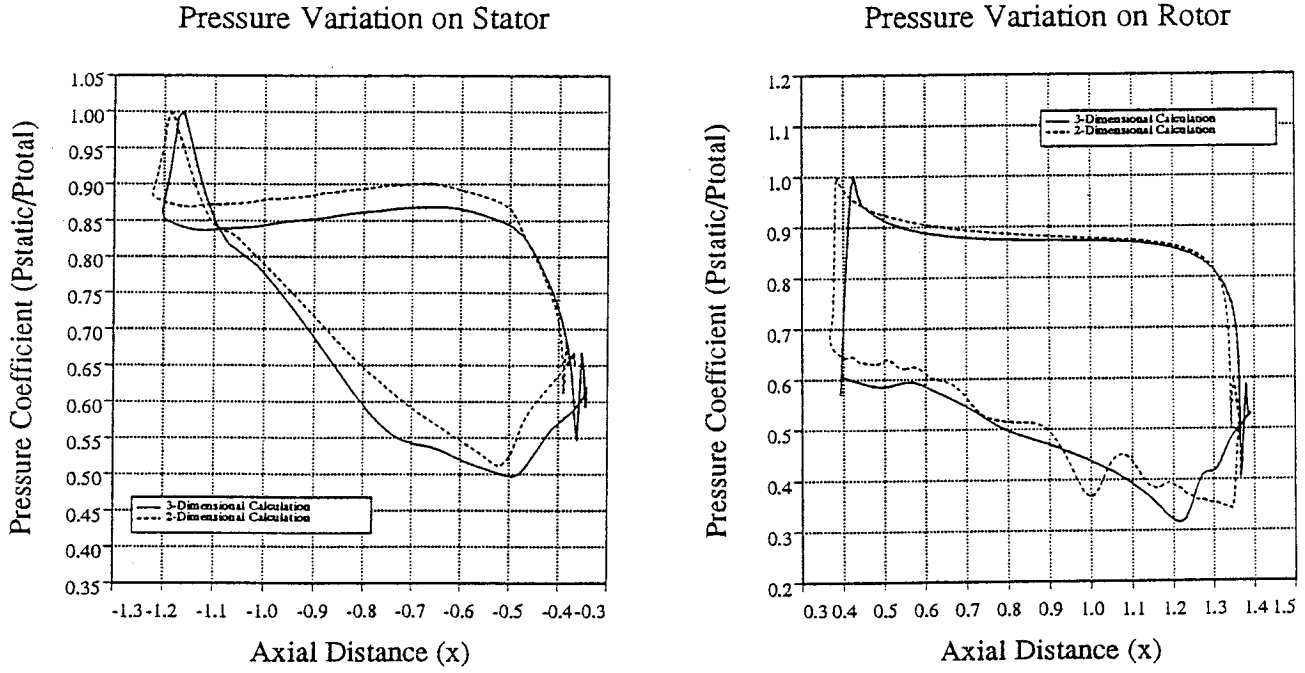

Fig. 9 Comparision between two- and three-dimensional predictions of time-averaged static pressures (a) stator and (b) rotor airfoil surfaces (Mid-span).

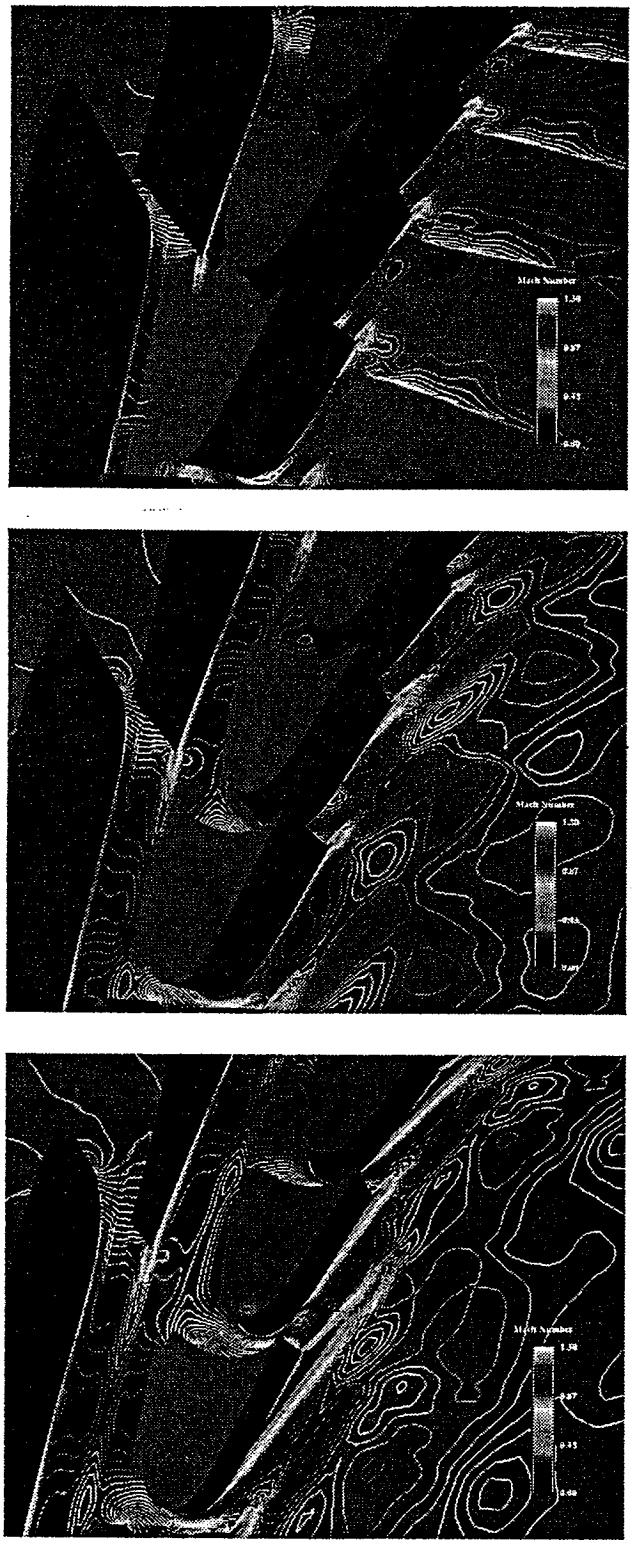

Fig. 10 Instantaneous contours of Mach number at (a) 20% span, (b) 50% span and (c) 80% span.

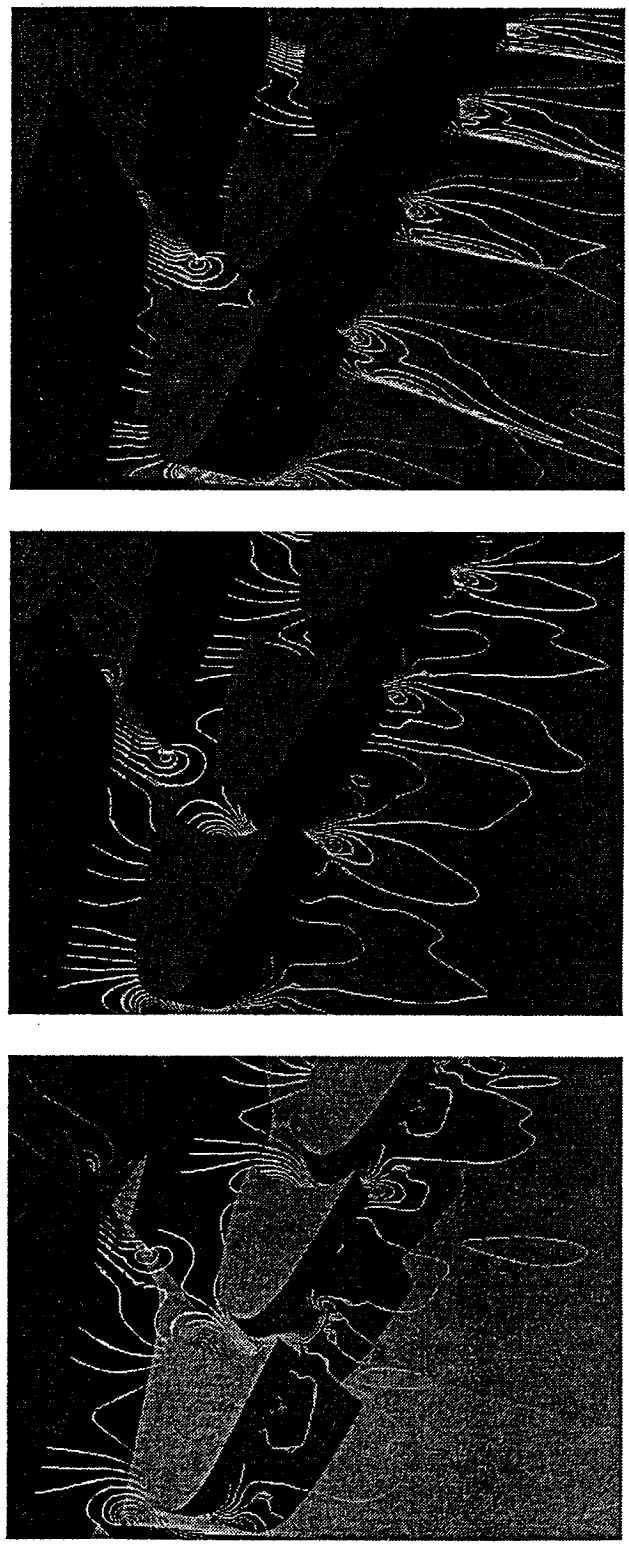

Fig. 11 Instantaneous contours of pressure at (a) 20% span, (b) 50% span and (c) 80% span.

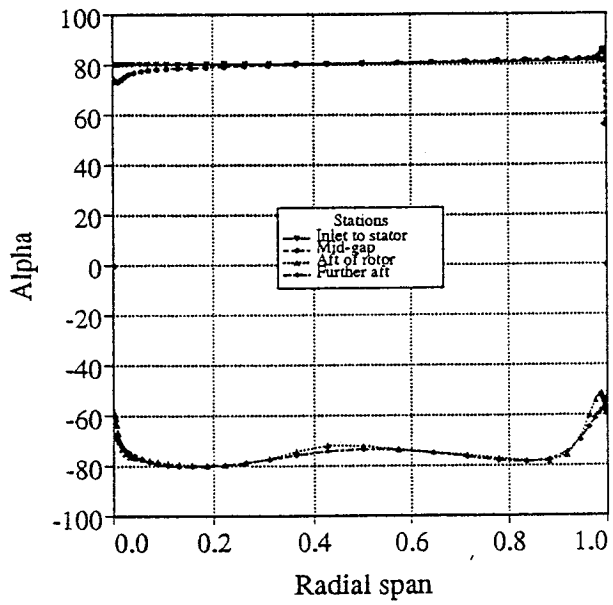

Fig. 12 Mass-averaged meridonial angle as a function of span.

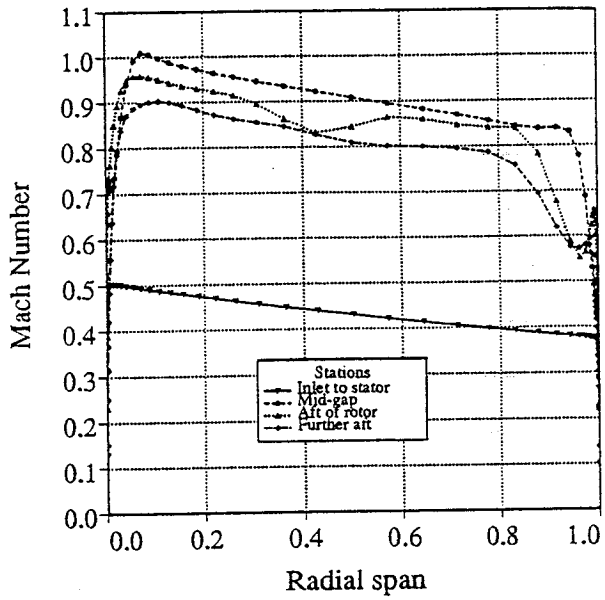

Fig. 14 Mass-averaged absolute mach number as a function of span.

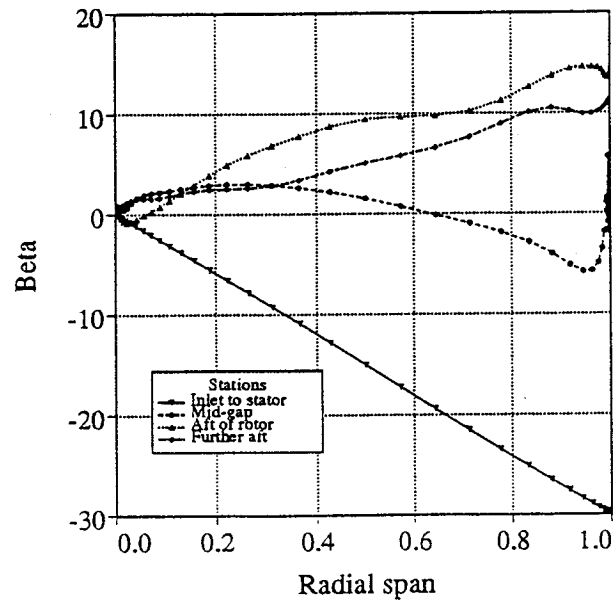

Fig. 13 Mass-averaged pitching angle as a function of span.

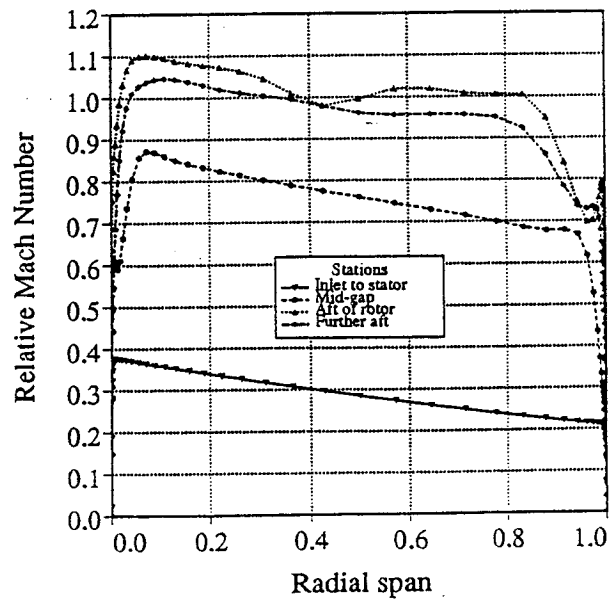

Fig. 15 Mass-averaged relative mach number as a function of span.

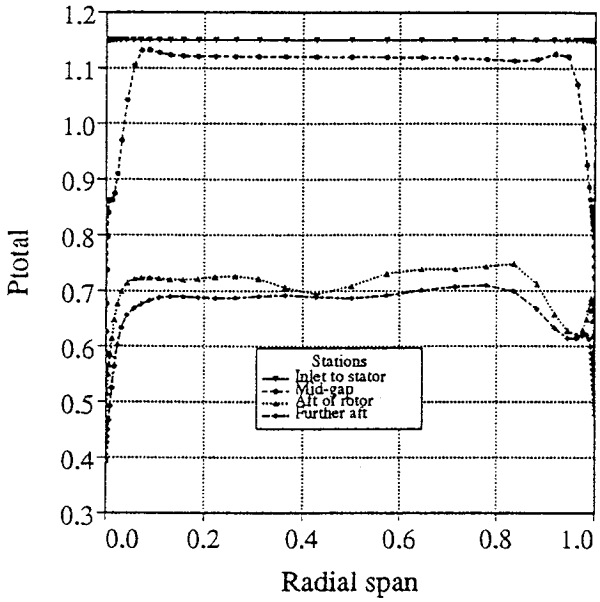

Fig. 16 Mass-averaged absolute total pressure as a function of span.

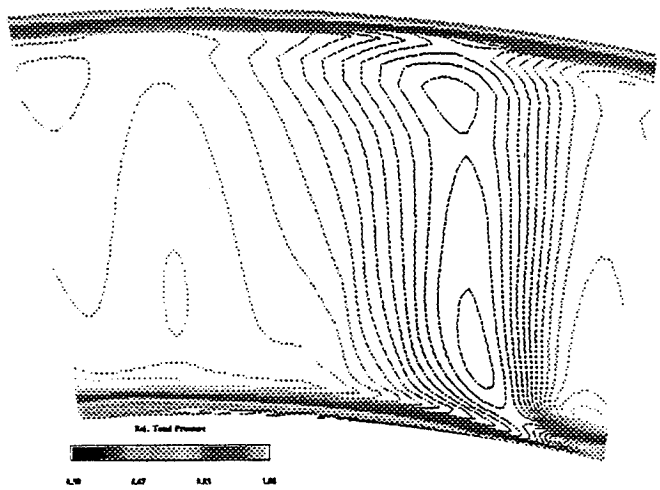

Fig. 18a Time-averaged relative rotational total pressure at mid-gap.

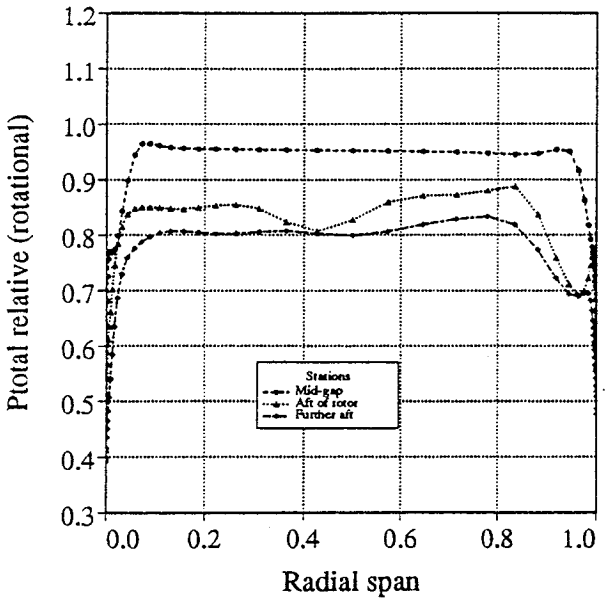

Fig. 17 Mass-averaged relative rotational total pressure as a function of span.

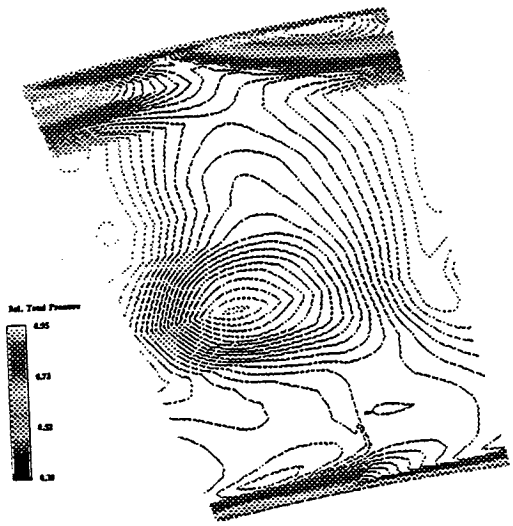

Fig. 18b Time-averaged relative rotational total pressure aft of the rotor airfoil.

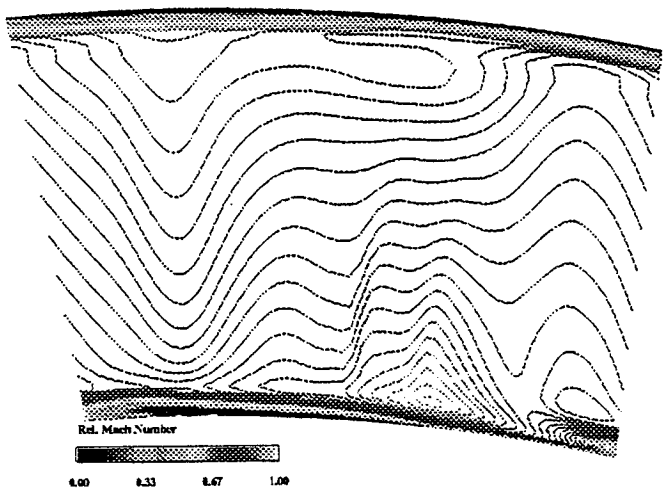

Fig. 19a Time-averaged relative mach number at mid-gap.

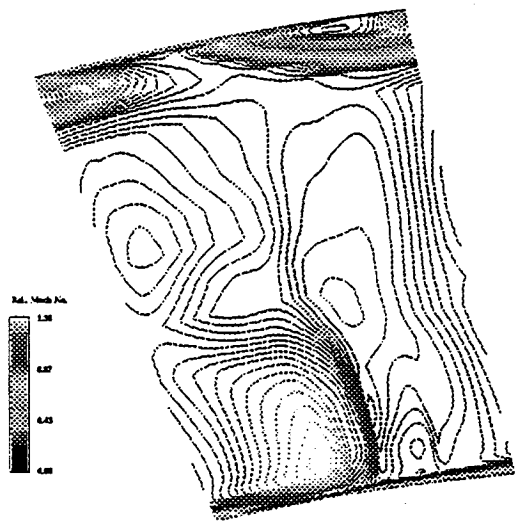

Fig. 19b Time-averaged relative mach number aft of the rotor airfoil.